universität wien

MASTERARBEIT / MASTER'S THESIS

Titel der Masterarbeit / Title of the Master's Thesis

„In Silico Investigation of Zirconocene-catalyzed Etherification Reactions: The Role of Triflate Ligands."

verfasst von / submitted by

Jan Brossette, B.Sc.

angestrebter akademischer Grad / in partial fulfilment of the requirements for the degree of

Master of Science (MSc)

Wien, 2023 / Vienna 2023

Studienkennzahl lt. Studienblatt / degree programme code as it appears on the student record sheet:	UA 066 862
Studienrichtung lt. Studienblatt / degree programme as it appears on the student record sheet:	Masterstudium Chemie
Betreut von / Supervisor:	Univ.-Prof. Dr. Dr. h.c. Leticia González
Mitbetreut von / Co-Supervisor:	Dr. Boris Maryasin

Acknowledgements

I would like to express my sincere gratitude to Univ.-Prof. Dr. Dr. h.c. Leticia González for supervision of my master's thesis and support throughout my scientific journey.

Furthermore, I would like thank wholeheartedly Dr. Boris Maryasin and Ricardo Meyrelles for patiently teaching me, and showing me the world of computational chemistry. Their unwavering support and valuable assistance throughout the thesis process, including the review and corrections, have been truly appreciated.

Additionally, I wish to express my profound appreciation to Denis Hoxha, Monika Schett, and Dr. Markus Oppel for their remarkable support in system administration and administrative work.

I owe a debt of gratitude to David Hernández-Castillo for his warm introduction to the group and guidance during my first steps into the field of quantum chemistry, and I am thankful to Dilara Farkhutdinova for her valuable support in creating visualizations.

Also, I want to acknowledge Dr. Daniel Kaiser, Dr. Tomislav Piteša and Dr. Saad Shaaban, for their invaluable contributions through corrections and engaging discussions, which significantly improved the quality of this project.

I extend my gratitude to Dr. Patrick Zobel for providing inspiring literature that enriched my research journey.

I am thankful to all the group members, including Dr. Štěpán Sršeň, Dóra Vörös, Dr. Boris Maryasin, Dr. Markus Oppel, Dr. Tomislav Piteša, Richard Jacobi, Univ.-Prof. Dr. Dr. h.c. Leticia González, Simon Tippner, Madlen Maria Reiner, Nadja Katharina Singer, Brigitta Bachmair, David Hernández-Castillo, Rahul Kumar Jingar, Ricardo Meyrelles, Sascha Mausenberger, Severin Polonius, Lorenz Grünewald, Dr. Sebastian Mai, Dr. Patrick Zobel, and Maximilian Xaver Tiefenbacher. Your contributions collectively created an enriching and positive working atmosphere that greatly enhanced my learning and research experience.

Last but certainly not least, I extend my heartfelt gratitude to Nadja Zeillinger for her unwavering and tirelessly support in matters of language, formatting, and constant inspiration throughout my entire master's studies.

1 Abstract

The direct nucleophilic substitution of alcohols has long piqued the interest of chemists, despite its inherent challenges. The Lundberg research group has achieved breakthroughs in this research field by unveiling a water-tolerant zirconocene triflate catalyst that effectively promotes this reaction. Nevertheless, the precise mechanism governing this reaction has remained elusive, prompting this computational investigation. Density functional theory and coupled cluster-based methods were employed to investigate the catalytic system. The results indicate that the catalyst does not follow either an S_N1 or S_N2-like pathways, which have been observed in similar systems documented in the literature. Furthermore, the mechanistic pathway involving the replacement of a hydroxy group with a triflate moiety followed by an attack from another alcohol was found to be unlikely as well. In contrast, the study underlines triflic acid's ability to serve as a catalyst for the described etherification reaction. Consequently, this computational inquiry endorses a mechanism that centers around the hydrolysis of the complex, resulting in the formation of triflic acid, which then acts as the actual catalyst for the reaction.

2 Zusammenfassung (German Version of Abstract)

Die direkte nucleophile Substitution von Alkoholen stellt bis heute eine herausfordernde Aufgabe für Chemiker dar. Nichtsdestotrotz konnte die Arbeitsgruppe um Helena Lundberg nennenswerte Fortschritte auf diesem Gebiet erzielen. Diese war in der Lage einen wassertoleranten Zirkonocentriflat-Katalysator zu verwenden, um Alkohole direkte nucleophile zu substituieren. Der Mechanismus, der experimentell noch nicht aufgeklärt werden konnte, wurde im Folgenden theoretisch untersuchen. Dazu wurden auf Dichtefunktionaltheorie und Coupled Cluster basierende Methoden verwendet, um das katalytische System zu modellieren. Diese Untersuchungen, konnten zeigen, dass der Katalysator vermutlich weder einer S_N1- noch einer S_N2-ähnlichen Reaktion folgt, wie sie in der Literatur für ähnlichen Systemen beobachtet wurdet. Außerdem konnte festgestellt werden, dass die Substitution der Hydroxy-gruppe durch ein Triflat Funktionalität, durch den Zirconiumkomplex energetisch unattraktiv zu sein scheint. Dagegen unterstreicht die Studie die Fähigkeit von Triflinsäure als Katalysator für die beschriebene Veretherungsreaktion zu dienen. Was vermuten lässt, dass Zirkonocentriflat hydrolysiert wird und Triflinsäure als aktive Katalysatorspezies freisetzt.

3 List of Abbreviations and Symbols

Å	Ångstrøm
ΔG_{373}	Gibbs free energy at 373K
°	degree
°C	Degree Celsius
‡	transition state
B3LYP	the hybrid density functional including Becke's three-parameter exchange functional and Lee-Yang-Parr's correlation functional
B97	Becke's 1997 hybrid density functional
BnOH	benzylalcohol
BTF	trifluorotoluene
cal	calorie
CC	coupled cluster
CCD	coupled cluster with double excitations
CCSD	coupled cluster with single and double excitations
CCSD(T)	coupled cluster with single, double and perturbative triples excitations
Cp	cyclopentadiene
CPCM	conductor-like polarizable continuum model
D2	second version of Stefan Grimme's dispersion correction
D3	third version of Stefan Grimme's dispersion correction
def2-SVP	Basis sets of Ahlrichs and coworkers with split valence polarization
def2-SVPD	Basis sets of Ahlrichs and coworkers with split valence polarization with diffuse functions
def2-TZVP	Basis sets of Ahlrichs and coworkers with valence triple-zeta polarization
DFT	density functional theory
DLPNO	domain-based local pair natural orbital
E	energy
E_{tot}	total energy
E_{MF}	mean field energy
E_{disp}	dispersion energy
f	Fock operator
GFN-FF	non-covalent interactions force field
GGA	generalized gradient approximation
$\hat{H}$	Hermitian operator
HF	Hartree–Fock
J	Joule
K	Kelvin
KS	Kohn–Sham

L	liter
M	transition metal
MC	Monte Carlo
MD	molecular dynamics
mGGA	meta generalized gradient approximation
MM	molecular mechanics
mol	mole
MP	Møller–Plesset
MP2	second order Møller–Plesset
NBO	natural bond orbital
Nu	nucleophile
OMs	mesylates
OTf	triflate
PBE0	hybrid functional of Perdew, Burke and Ernzerhof
PES	potential energy surface
PhEtOH	2-phenylethanol
r	radius
SD	Slater determinant
SIE	self interaction error
SMD	solvent model density
SP	single point
T	excitation operator
THF	tetrahydrofuran
T_S	Kohn–Sham kinetic energy
TS	transition state
V_{xc}	exchnage correlation energy functional
Z	nuclear charge
λ	variable
ρ	density
Ψ	wavefunction
ωB97XD	range-separated version of Becke's 97 functional with additional dispersion correction

Contents

4 Introduction

The pursuit of discovering novel transformations or enhancing existing ones has always been a central focus for synthetic chemists. As the need for environmentally friendly solutions becomes increasingly urgent due to worldwide problems, such as climate change, the discovery of new sustainable reactions has taken on even greater importance. Highlighted by the ACS Green Chemistry Institute Pharmaceutical Roundtable as a chemical transformation that would benefit from improvements in process greenness is the direct substitution of alcohols.[1] In this challenging reaction, the displacement of a hydroxyl group is carried out, resulting in the generation of water as the sole by-product. Owning to the inherent thermodynamic and kinetic barriers, the substitution of hydroxyl groups is typically accomplished indirectly by converting the alcohol into a suitable leaving group, such as a halide or a sulfonate ester (see Figure 1 **a**), followed by substitution of the leaving group with a nucleophile (Nu^-). In general, the activation towards an S_N2 type displacement in this reaction is typically unfavourable due to the involvement of additional reaction steps and its negative impact on atom economy.[2] Besides the substitution of the alcohol with a good leaving group, various catalytic strategies have been employed to substitute hydroxyl moiety. A catalyst-based strategy for hydroxyl group displacement centers around the concept of borrowing hydrogen, frequently necessitating the presence of a transition metal (M) (see Figure 1 **b**).[3] In this transformation, an alcohol (**1**) undergoes dehydrogenation, leading to the formation of an aldehyde or ketone (**2**). This intermediate is then subsequently condensed with an amine (**3**)[4] or, in more recent applications, with carbon nucleophiles.[5] Following this, the unsaturated product (**4**) is subjected to reduction using the previously formed catalyst's hydride leading to (**5**). Methodologies for an S_N1 reaction pathway are diverse, with numerous examples of both Brønsted and Lewis acids serving as catalysts (see Figure 1 **c**). Common species of Lewis acids are bivalent, or trivalent metal triflates (OTF^-).[6, 7, 8] Moreover, exploration of group IV metal analogues has been relatively rare.[9] The research group of Lundberg has made significant strides by demonstrating that the commercially available $ZrCp_2OTf_2 \cdot THF$ can also serve as a catalyst in this transformation. Notably, this complex exhibits moisture tolerance, setting it apart from most other Lewis acids, and can be handled without requiring any water removal techniques. Even more surprisingly, the zirconium complex is only able to catalyze the reaction when water is present in the reaction mixture (see Figure 1 **d**).[10] Moreover, the group of Lundberg successfully utilized this catalyst to convert biomass, namely the monomers of lignin, into potential precursors for bioplastic or thermosets.[11]
Nonetheless, despite experimental efforts to investigate, the exact reaction mechanism using ($ZrCp_2OTf_2 \cdot THF$) as a catalytic species remains unknown. Hence, the objective of this master's thesis is to elucidate the mechanism of the reaction through a computational approach, aiming to address the numerous unanswered questions surrounding this intriguing catalytic system. Especially the unique role of the OTf ligands and role of water during the reaction is investigated. Notably, $ZrCp_2Cl_2$, shows no reactivity towards the alcohols,[10] highlighting the crucial influence of OTf in the catalytic process.

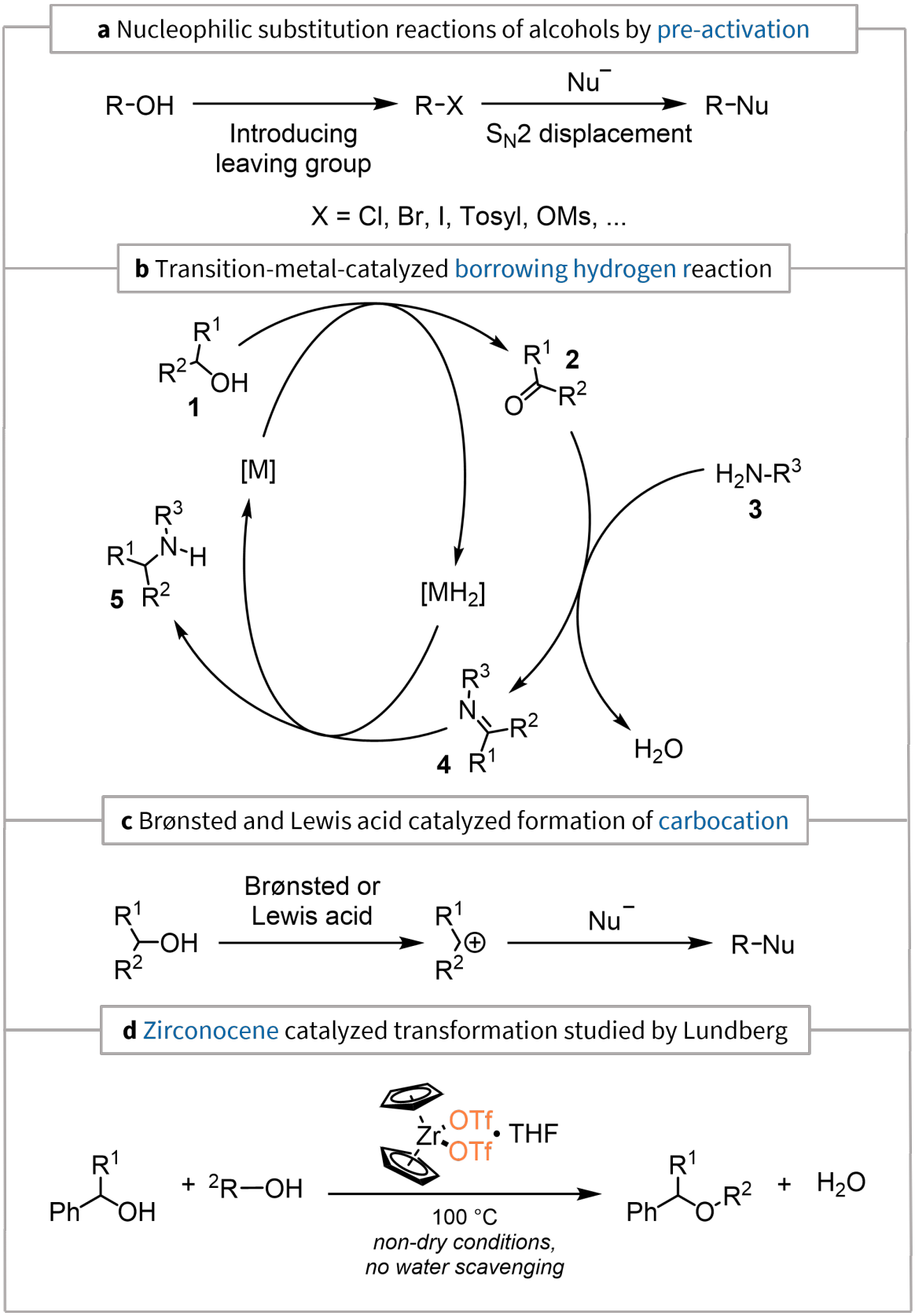

Figure 1: **a** Nucleophilic substitution reactions of alcohols by pre-activation; **b** Transition metal (M) catalyst borrowing hydrogen reaction; **c** Direct catalytic substitutions via S_N1 mechanism; **d** Recent discoveries by Lundberg and coworkers.[10]

5 Theoretical background

5.1 Hartree-Fock

For many years, traditional wave function based approaches have been the method of choice when performing electronic structure calculations on chemical systems. The most elemental one is the Hartree-Fock (HF) method from the late 1920s.[12] An N electron wave function Ψ, subject to the HF theory and the Pauli principle can be mathematically represented by a Slater determinant (SD) (Equation 1).

$$\Psi_{\text{SD}}(x_1, x_2, \ldots, x_N) = \frac{1}{\sqrt{N!}} \begin{pmatrix} \chi_1(x_1) & \chi_2(x_1) & \cdots & \chi_N(x_1) \\ \chi_1(x_2) & \chi_2(x_2) & \cdots & \chi_N(x_2) \\ \vdots & \vdots & \ddots & \vdots \\ \chi_1(x_N) & \chi_2(x_N) & \cdots & \chi_N(x_N) \end{pmatrix} \tag{1}$$

The spin-orbitals (χ) in the SD can then be variationally optimized to give the SD with the lowest expected value of energy. The final equations for the optimized spin-orbitals suggest that the approximating of the *N*-electron wave function by a single SD has lead to the picture that each electron "feels" the mean field of other electrons in the molecule, instead of directly interacting with each of them. This is why the HF method is usually leading to poor results since effects of electron correlation is neglected. However, electron correlation can be addressed using so-called post-HF methods.[13]

5.2 Møller–Plesset perturbation theory

An early attempt by Christian Møller and Milton S. Plesset to account for electron correlation effects by means of Rayleigh–Schrödinger perturbation theory (RSPT) within the wave function dates back to 1934.[14]. The basic idea of RSPT is to partition the Hamiltonian ($\hat{H}$) into an unperturbed Hamiltonian ($\hat{H}^0$) (also called reference) and a perturbed Hamiltonian ($\hat{H}^1$) (see Equation 2). λ is used as a dummy parameter to track the correction order and is in the end set to 1.

$$\hat{H} = \hat{H}^0 + \lambda \hat{H}^1 \tag{2}$$

The energy and wave function of the system can be expressed as shown below (for the energy, see Equation 3, and for the wave function, refer to Equation 4). Here, E^0 and Ψ^0 represent the eigenvalue and eigenfunction of $\hat{H}_0$, while E^n and Ψ^n denote the *n*-th order perturbation corrections to the energy and the wave function. These correction formulas are obtained by substituting the perturbative forms of $\hat{H}$, $\hat{E}$, and Ψ into the Schrödinger equation.

$$E_{exact} = E_0 + \lambda^1 E_1 + \lambda^2 E_2 + \lambda^3 E_3 + \cdots \tag{3}$$

$$\Psi = \Psi_0 + \lambda^1\Psi_1 + \lambda^2\Psi_2 + \lambda^3\Psi_3 + \cdots \tag{4}$$

In Møller–Plesset perturbation theory, ($\hat{H}^0$) is the sum of Fock operators (see Equation 5) and ($\hat{H}^1$) the difference between ($\hat{H}$) and ($\hat{H}^0$) (see Equation 6).

$$\hat{H}^0 = \sum_{i=1}^{N} \hat{f}'(i) \tag{5}$$

$$\hat{H}^1 = \hat{H} - \hat{H}^0 \tag{6}$$

MP*n* energies and wave functions correspond to RSPT energies and wave functions up to the *n*-th order. For example, the MP2 energy is the sum of zeroth, first, and second-order perturbations energies. It's worth noting that MP1 is an identical method to the HF method, which implies that only MP2 or higher orders of perturbations are considered more accurate than HF. This is because they incorporate electronic correlation, progressively improving the accuracy of energy representations in accordance with the order of perturbation. [15, 16]

5.3 Coupled-cluster methods

A commonly used post-Hartree–Fock method is the coupled cluster (CC) approach. CC theory relies on a generalized wave function expressed as a combination of SDs. However, the method allows to include all correlations of a given type to infinite order, by applying the excitation $\hat{T}$ operator. The number of electrons is represented by *n* (see Equation 7).

$$\hat{T} = \hat{T}_1\,, \hat{T}_2\,, \hat{T}_3, \ldots, \hat{T}_n \tag{7}$$

The general expression for a wavefunction, where Ψ_0 is HF wave function and *N* is the number of electrons, according to the CC approach is shown in Equation 8.

$$\Psi_{\text{CC}} = Ne^{\hat{T}} \left(1 + \hat{T} + \frac{\hat{T}^2}{2} + \frac{\hat{T}^3}{6} + \cdots\right) \Psi_0 \tag{8}$$

The CC method is computationally demanding, and its cost grows rapidly with the size of the system and the level of excitation included. Therefore, truncation of the order of expansion is needed. Since including only the $\hat{T}_1$ would not give any improvement over HF, the lowest level of approximation is $\hat{T} = \hat{T}_2$ (CCD). Since both CCSD and CCD scale with the factor same factor in the limit of a large basis set, CCSD is usually preferred over CCD. Furthermore, the CCSD method can be expanded to a Taylor series due to its exponential ansatz, yielding Equation 9.

$$\Psi_{\text{CCSD}} = N \left(1 + \hat{T}_1 + \hat{T}_2 + \frac{\hat{T}_1^2}{2} + \hat{T}_1\hat{T}_2 + \frac{\hat{T}_2^2}{2} + \frac{\hat{T}_1^3}{6} + \cdots\right) \Psi_0 \tag{9}$$

As one can see from Equation 9, CCSD includes single ($\hat{T}_1$) and double ($\hat{T}_2$, or double of application of $\hat{T}_1$), and triple ($\hat{T}_1^3$ and $\hat{T}_1, \hat{T}_2$) excitation and so on. Moreover, the CCSD(T) method, which includes perturbation theory for triple excitation, is often referred to as the gold standard of quantum chemistry, due to its high accuracy.[16]
Among the most popular approaches to overcome the computational cost, but retain chemical accuracy is the domain-based local pair natural orbital (DLPNO) method, developed by Frank Neese and co-workers.[17] Reduced computational demand is achieved by classifying electron pairs as either weakly or strongly correlated. Strongly correlated pairs are treated with the CC approach, while for weakly correlated pairs MP2 is employed. The energy obtained by MP2 is added subsequently to the correlation energy. However, so far it is not possible to use the DLPNO approach to perform geometry optimization or frequency calculations. Only single point energies can be obtained by that method.[17]

5.4 Density functional theory

One downside of Post-Hartree–Fock methods is their huge computational effort. This makes their application for large and complex systems almost impossible. Density functional theory (DFT) attempts to address both the high computational demands of post-HF methods and the inaccuracy of HF by replacing the many-body electronic wave function with the electronic density as the basic quantity. Whereas, for an N electron system, wave functions contain $4N$ variables (three spatial and one spin coordinate for each electron), the electron density is a function of only 3 degrees of freedom and has the same number of variables, independent of the system size.[15]

5.4.1 Hohenberg–Kohn theorems

DFT, as it is recognized today, is theoretically based on the two Hohenberg–Kohn theorems.[18] The first theorem states that the energy and all ground-state properties of an electronic system are uniquely determined by the electron density.
The second theorem establishes that the density obeys a variational principle. Thus, the problem of solving the many-body Schrödinger equation is bypassed, and the objective becomes to minimize a density functional. Expectation values obtained through the variational principle are always higher or equal to the true energy.[13]

5.4.2 Kohn–Sham equations

However, one should bear in mind that the Hohenberg-Kohn theorems, while fundamental in concept, do not offer a direct approach for solving the necessary equations to compute molecular properties. Early approaches to compute these properties only used the electron density itself as an input. However, these approaches were lacking the description of the kinetic energy of the electronic energy. Walter Kohn and Lu Jeu Sham introduced a different approach, which is the

common current realization of DFT. In the Kohn–Sham (KS) approach orbitals are introduced to overcome the poor representation of the kinetic energy, which leads to Equation 10, which makes it possible to compute the energy of the system.

$$E[\rho(r)] = \underbrace{\frac{1}{2}\iint \frac{\rho(r_1)\rho(r_2)}{r_{12}}\, dr_1\, dr_2}_{\text{Coulombic repulsion between electrons}} + \underbrace{T_S[\rho(r)]}_{\text{kinetic energy associated with the orbital}} \underbrace{- \sum_J \left(\int \frac{\rho(r) Z_J}{r_J} \right) dr}_{\text{Coulombic energy interaction between nuclei and the electron density}} + \underbrace{V_{xc}[\rho(r)]}_{\text{exchange-correlation energy functional}} \tag{10}$$

The equation consists of four main terms: the Coulombic repulsion energy between electrons, the kinetic energy associated with the orbital, the Coulombic energy interaction between nuclei and the electron density, and the exchange-correlation energy functional. The first three terms are relatively straightforward to calculate. However, the mathematical challenge lies in the fourth part, as the exact form of this functional is not known. Subsequently, leading to the development of various approximations. [16]

5.4.3 Hybrid functionals

A major source of error in Kohn-Sham Density Functional Theory (KS-DFT) is the self-interaction error (SIE). This error arises from the inability of functionals to precisely counteract self-Coulomb and self-exchange-correlation effects across all one-electron densities. Among the approximations for exchange-correlation energy functionals, hybrid functionals have gained significant popularity. Unlike less accurate functionals such as the Generalized Gradient Approximation (GGA) and meta-GGA (mGGA), hybrid functionals replace a portion of the approximate DFT exchange with Fock exchange, which mitigates the SIE. Furthermore, the famous and widely used B3LYP[19, 20] functional also belongs to the class of hybrid functionals. However, it's important to note that the SIE is not completely eliminated by the hybrid functional approximation.[13]

5.5 Dispersion correction

Due to the intrinsic SIE of KS-DFT, non covalent interactions, especially London dispersion interactions are described incorrectly. Therefore, dispersion corrections are undeniably necessary for theoretical simulations to reach sufficient accuracy. Many different approaches were made to replicate dispersion interactions. A still widely used approach was proposed by Grimme in 2006, the D2 method, which belongs to the group of semiclassical treatments. In semiclassical treatments the dispersion energy (E_{disp}) between atom pairs is added to the electronic energy of the mean-field (E_{MF}) (e.g., DFT) approach, yielding the total energy (E_{tot}) as shown in Equation 11.[21]

$$E_{tot} = E_{MF} + E_{disp} \tag{11}$$

The D2 method is regarded as a fully empirical correction, and therefore does not contain any dependence on the molecular environment. D3[22] the successor of the D2 method takes the molecular environment into count and is therefore the state-of-the-art method. Historically, the D2 method was proposed to be applied in combination with the nonhybrid variant of the B97 functional.[23] The good interplay between D2 and B97 has also been exploited by Chai and Head-Gordon in the development of the range-separated hybrid functional ωB97XD, which is still popular until today.[24, 25]

5.6 Solvation

To properly describe chemical systems computationally it is important to include as many environmentally related effects as possible. One of these effects is the interaction of the molecule with the solvent. Mainly two different approaches are used to model these interactions: One of these is explicit solvation, where every solvent molecule is modeled atomistically. This treatment is a more intuitively realistic picture of the studied systems but comes along with a big computational cost. Therefore, explicit solvation is only feasible in MM (molecular mechanics), MD (molecular dynamics), or Monte Carlo (MC) simulations. A computationally less demanding method is implicit solvation. In this approach, the solute is situated within a cavity with a shape roughly resembling the molecule, while the solvent is represented as a continuous medium with a specfic dielectric constant. [13] Two commonly used implicit solvation models are SMD[26] (Solvent Model Density) and CPCM[27, 28] (Conductor-like Polarizable Continuum Model). While CPCM models the solute cavity by creating overlapping spheres, SMD takes a different approach by utilizing the complete solute electron density to compute the cavity-dispersion contribution, instead of solely relying on the surface area. A compromise between explicit and implicit solvation is micro solvation, where only some solvent molecules are described explicitly, while still an implicit solvation model is applied to the whole system. Usually, in reactions where solvent molecules are directly included in the reaction micro solvation is used.[29]

5.7 Conformational search

Exploring the conformational space of a molecule is of paramount importance. The energy landscape of flexible molecules often includes low-lying conformers, which are hard to find intuitively. However, the most stable conformers dictate the reactivity of molecules and therefore are important to consider. Furthermore, in some cases different conformers can lead to different reaction pathways, thus resulting in varying selectivity. The conformational search in this study was done according to Figure 2. Initially, meta dynamic simulations were employed using non-covalent interactions forcefield (GFN-FF)[30] to obtain a set of initial structures. Subsequently, the single-point (SP) energies of these structures were computed using DFT calculations, and they were ranked based on their energetic stability. To further refine the selection, any structure with an energy that

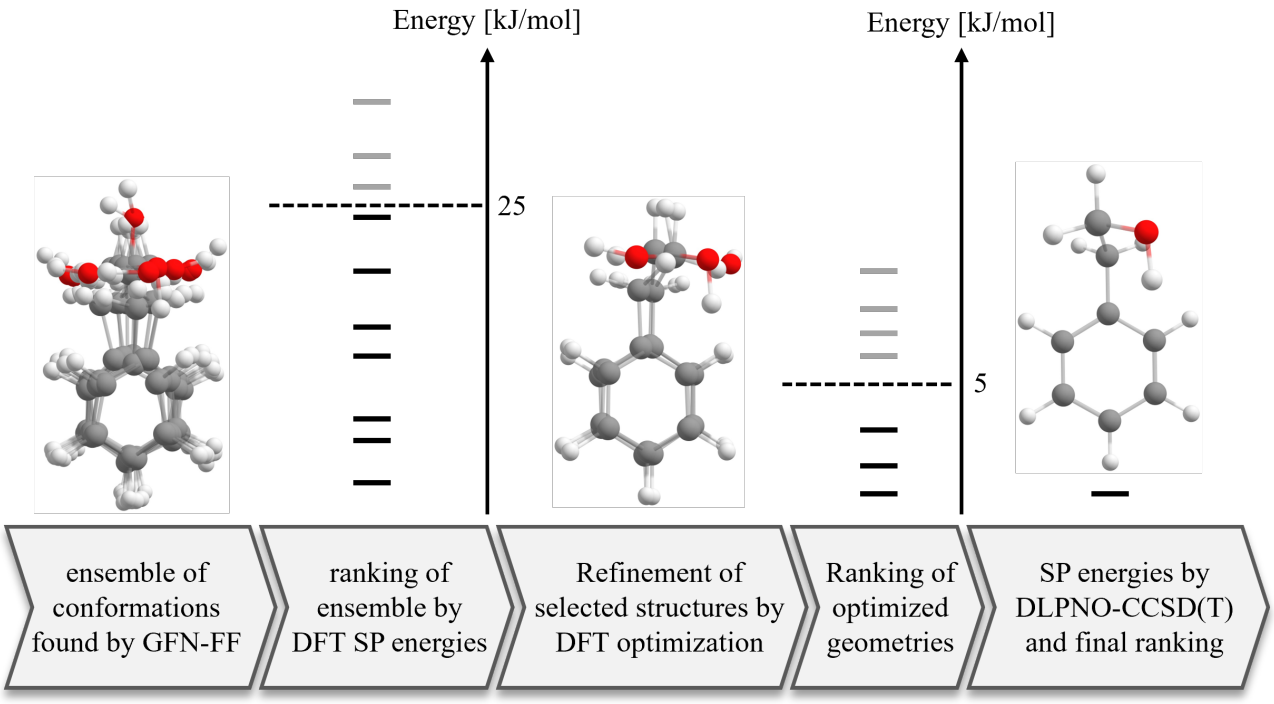

Figure 2: Workflow of the performed conformational search, with benzyl alcohol as example substrate. Gray – neglected conformers, black – further considered conformers.

is 25 kJ/mol higher than the most energetically favorable conformer was excluded from further consideration. The remaining conformers were subjected to geometric optimization and ranked again, considering thermal correction terms obtained through frequency calculations of the optimized geometries. Conformers that were only 5 kJ/mol or less high in energy than the most stable structure were further investigated. Hence, SP energies were calculated using the DLPNO-CCSD(T) method. The resulting energies were ranked, taking into account the thermal correction terms obtained from the frequency calculations performed at the DFT level applied for optimized geometries. Through this comprehensive approach, the most stable conformer was identified.

6 Computational details

All quantum chemical calculations determining structural and energetic properties at the DFT level of theory were performed using the Gaussian 16 software.[31] The ORCA 5.0.1 program package[32] was used to obtain energies by the DLPNO-CCSD(T) method.[17] To establish an appropriate theoretical framework for characterizing the studied system, a benchmark study was conducted. This involved a comparison of the following DFT functionals: ωB97XD[33, 34], PBE0-D3[35, 36, 37], and B3LYP-D3.[19, 38] Also, different basis sets, namely def2-SVP,[39] def2-SVPD,[40] and def2-TZVP[39] were applied. All calculations using PBE0 and B3LYP were performed including D3 dispersion correction with Becke-Johnson damping.[22]. Furthermore, CPCM[27, 28] and SMD[26] solvation model with parameters of toluene were included. For all molecules, which were considered during mechanistic studies, MTD simulations, based on the GFN-Force-Field (GFN-FF),[30] were employed to explore the conformational space of the molecules. To conduct this exploration, the software package Conformer-Rotamer Ensemble Sampling Tool (CREST) was used.[41, 42] The structures located with CREST have then been subjected to ωB97XD/def2-SVP[33, 34, 39] geometry optimization. The ωB97XD functional and the def2-SVP basis set were chosen because they showed the best performance among the different benchmarked levels of theory (for more details see section 7). To confirm that stationary points were obtained and to verify the nature of them, computations of harmonic vibrational frequencies were performed at the same level of theory as geometry optimizations. Final Gibbs free energies were obtained by the addition of single point energies calculated at the DLPNO-CCSD(T)/def2-TZVP[17] level of theory and the thermal corrections computed at ωB97XD/def2-SVP level of theory. All energies are reported in kcal/mol. Energy profiles were constructed using the most stable conformation (the global minimum) of each intermediate and transition state. Free energies in solution have been corrected for concentration effects (1 mol/L at 373 K), temperature (373 K), and quasi-harmonic corrections to both entropy and enthalpy, defaulting to the Grimme method for entropy[43] and the Head-Gordon enthalpy correction,[44] by using the programm GoodVibes.[45]. NBO charges[46, 47] were calculated from the ωB97XD/def2-SVP level of theory.

7 Results and discussion

7.1 Benchmark study

Considering the scarce literature dare of the studied system, a benchmark study was conducted prior to embarking on any mechanistic investigations. This preliminary analysis aimed to identify a reliable quantum mechanical modeling method that accurately and efficiently describes the investigated system. Therefore, DFT functionals, which have been used to study zirconocene complexes were compared. Among the most popular functionals are B3LYP,[48, 20] PBE0,[49, 50] and ωB97XD[51, 52]. Furthermore, the influence of the applied basis set was studied as well. Different basis sets of the "Karlsruhe family", namely def2-SVP, def2-SVPD, and def2-TZVP, were probed to see whether additional diffuse functions or a higher ζ-level affected the obtained results. In order to judge the performance of the different tested level of theories, optimized molecular geometries of $ZrCp_2Cl_2$[53] and $ZrCp_2OTf_2 \cdot THF$[54] have been compared to structures empirically obtained by X-ray crystal analysis. The following bonds, have been considered: Zr-Cl, Zr-center of mass of the Cp ligand (Zr-Cp), Zr-O of the OTf ligand (Zr-OTf), and Zr-O of THF moiety (Zr-THF). Figure 3 illustrates the absolute difference of the computed bond distances from the bond lengths observed in the X-ray structures (see Table 3 in the appendix for a tabulated presentation). The same kind of analysis was done for the bond angles Cl-Zr-Cl, Cp-Zr-Cp, and fTO-Zr-OTf. The results are shown in Figure 4 (see Table 4 in the appendix for a tabular representation).

All the tested functionals showed comparable results. Nevertheless, among the three functionals under consideration, B3LYP exhibited the worst performance. In particular, the Zr-Cp bond lengths are described less accurately in contrast to the other two functionals. Moreover, ωB97XD gave slightly better results for Zr-Cl, Zr-OTf bond lengths and fTO-Zr-OTf, Cl-Zr-CL bond angles compared to PBE0. Since Zr-Cl and Zr-OTf bonds are crucial in the undertaking study, ωB97XD was chosen to conduct the further computational work. Furthermore, additional diffuse functions or a higher ζ-level from double-ζ to triple-ζ in the basis set did not show a sharp increase in accuracy. Hence, the def2-SVP was chosen as the basis set owing to its low computational cost.

Also, the influence of different implicit solvation models (CPCM and SMD) was investigated. Therefore, the same computed bond lengths and angles as before were compared (see Figure 5, Figure 6 or Table 5, Table 6 in the apendix for tabulated presentation). SMD and the CPCM solvation model produced similar results, demonstrating their reliability. Additionally, the calculated geometric properties of the solvated complex closely matched the experimental values of the solid-state structure. Despite SMD being a more sophisticated model compared to CPCM, as it accounts for cavity creation effects, CPCM was used for further computational investigations. This choice was driven by convergence issues encountered when using SMD as a solvation model during transition state (TS) optimization. In contrast, CPCM smoothly yielded TS structures as stationary points, and both SMD and CPCM produced similar results regarding the geometric structure.

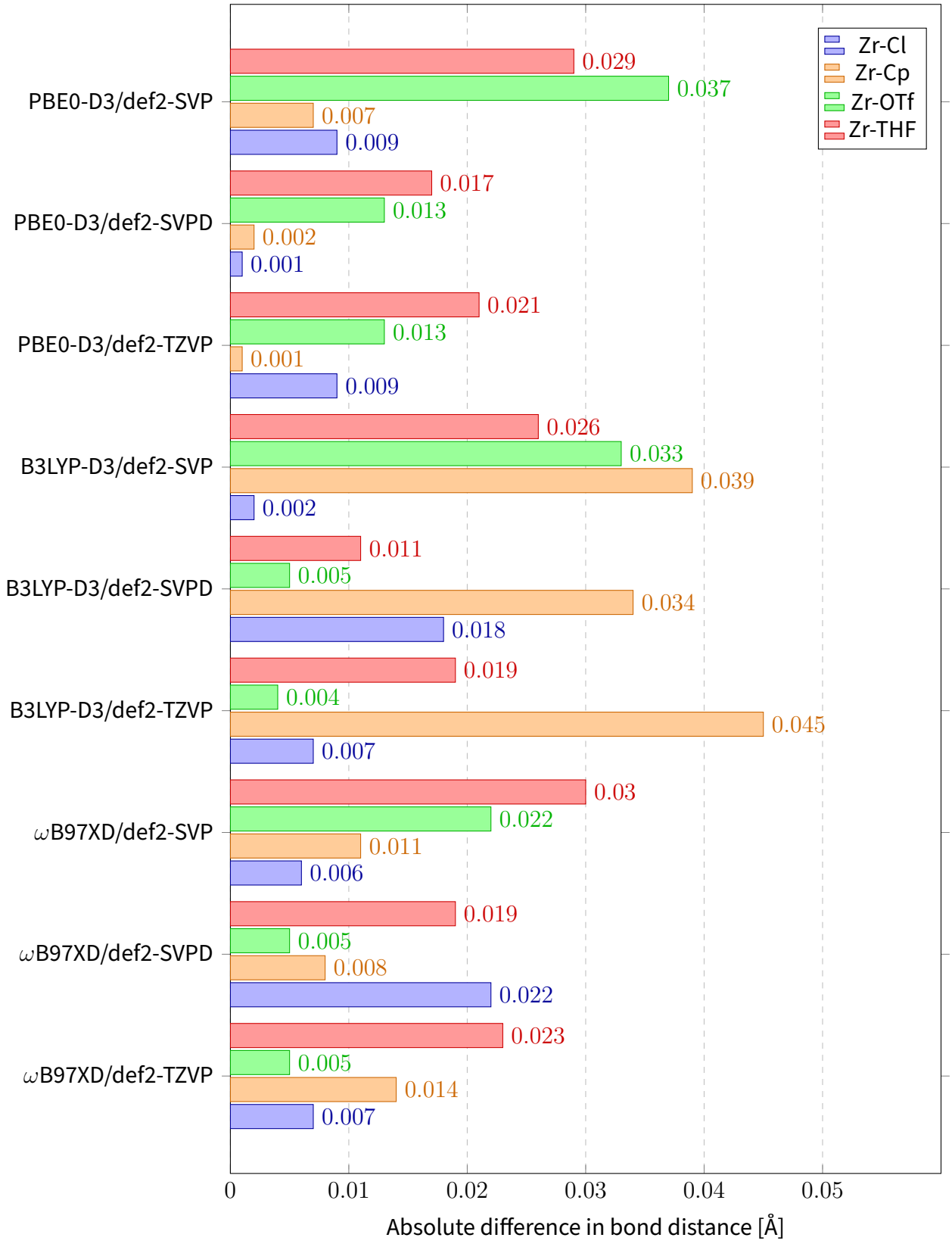

Figure 3: Absolute difference of experimentally (X-ray)[53, 54] measured and theoretically calculated Zr-Cl, Zr-Cp, Zr-OTf, and Zr-THF bond lengths at different levels of theory. (Solvation: CPCM toluene).

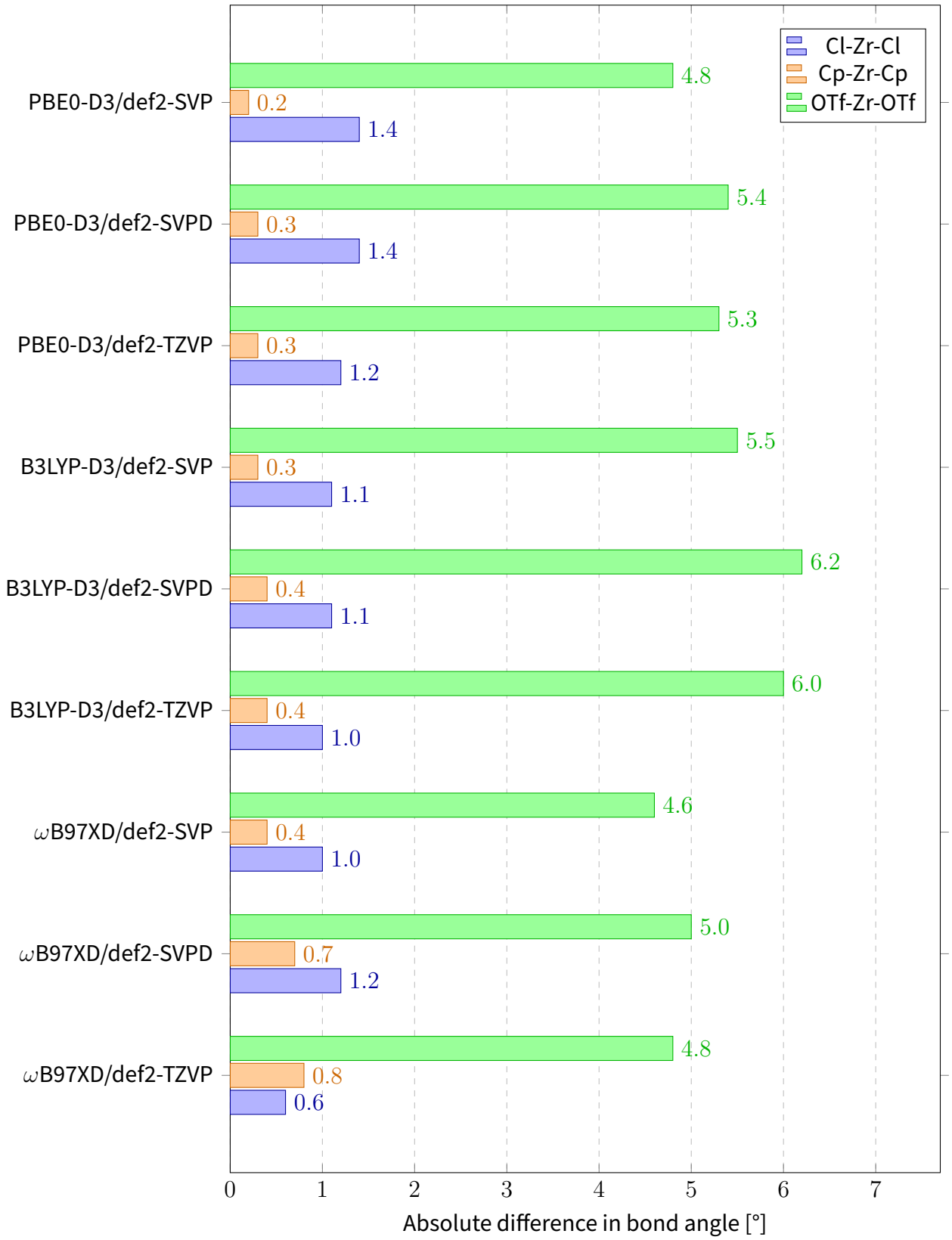

Figure 4: Absolute difference of experimentally (X-ray)[53, 54] measured and theoretically calculated Cl-Zr-Cl, Cp-Zr-Cp, and fTO-Zr-OTf bond angles at different levels of theory. (Solvation: CPCM toluene).

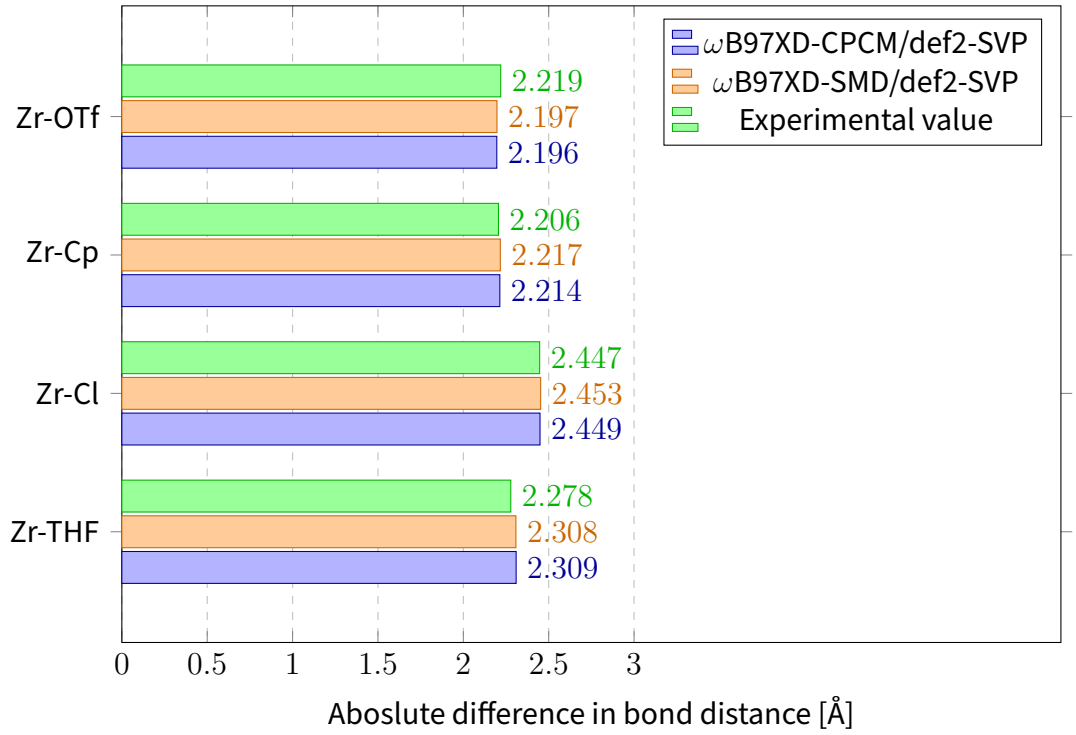

Figure 5: Experimentally (X-ray)[53, 54] measured and theoretically calculated Zr-Cl,Zr-Cp, Zr-THF, and Zr-OTf bond distances with different solvation models: CPCM and SMD (toluene); level of theory: ωB97XD/def2-SVP.

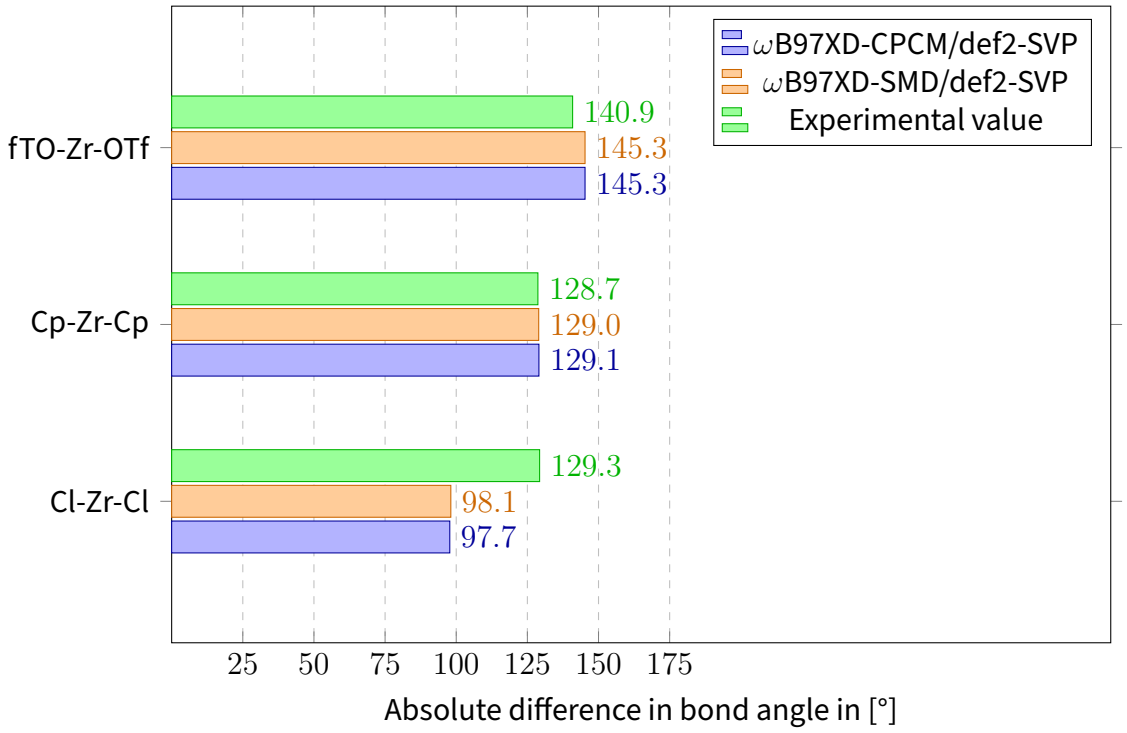

Figure 6: Experimentally (X-ray)[53, 54] measured and theoretically calculated Cl-Zr-Cl, Cp-Zr-Cp, and fTO-Zr-OTf bond angles with different solvation models: CPCM and SMD (toluene); level of theory: ωB97XD/def2-SVP).

7.2 Identifying the catalytic active species

The overall reaction for direct substitution of alcohols employed by the Lundberg group for kinetic analysis and general studies is shown in Figure 7.[10] Benzyl alcohol (BnOH) and 2-phenylethanol (PhEtOH) undergo a $ZrCp_2OTf_2 \cdot THF$ catalyzed reaction to produce the corresponding asymmetric ether (Bn-O-PhEt).

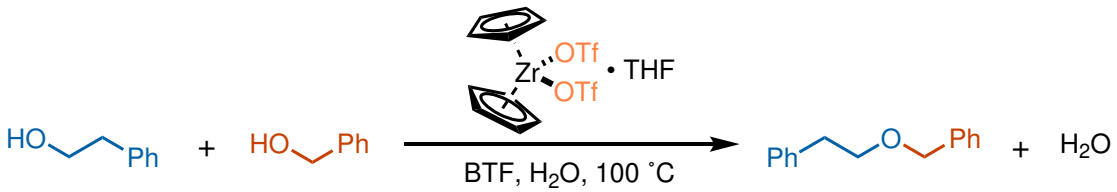

Figure 7: General reaction setup by the Lundberg group.

In the standard reaction setup, benzotrifluoride (BTF) serves as the solvent. However, due to limitations of the Gaussian 16 software package no well-parameterized dielectric constants were available for BTF, which is the actual solvent used in the experimental setup. Toluene was chosen as an appropriate substitute solvent for the computational simulations due to its chemical similarity to BTF. Moreover, BTF serves the purpose of suppressing Friedel–Crafts-like side reactions. It's worth noting that the reaction is also viable in toluene.
In order to investigate the mechanism, various potentially significant species were taken into consideration. As reported in the literature, triflate ligands are susceptible to facile exchange by water molecules.[55] Hence, a comparison was made among various plausible species that could arise during a ligand exchange reaction, with the aim of discerning the catalytically active entity. Also, the difference between the coordination of benzylalcohol (BnOH) and phenylethanol (PhEtOH) to the zirconocene complex was studied. In pursuit of this objective, a comparison was conducted involving the Zr bond distance to the oxygen atom of the coordinated alcohol, as well as the NBO charges of both Zr and the corresponding oxygen atom. Additionally, discrepancies in the total Gibbs free energies (ΔG) of the respective species were examined. Figure 8 shows the considered species in their Lewis Structure, while in Table 2 the computed result are displayed.

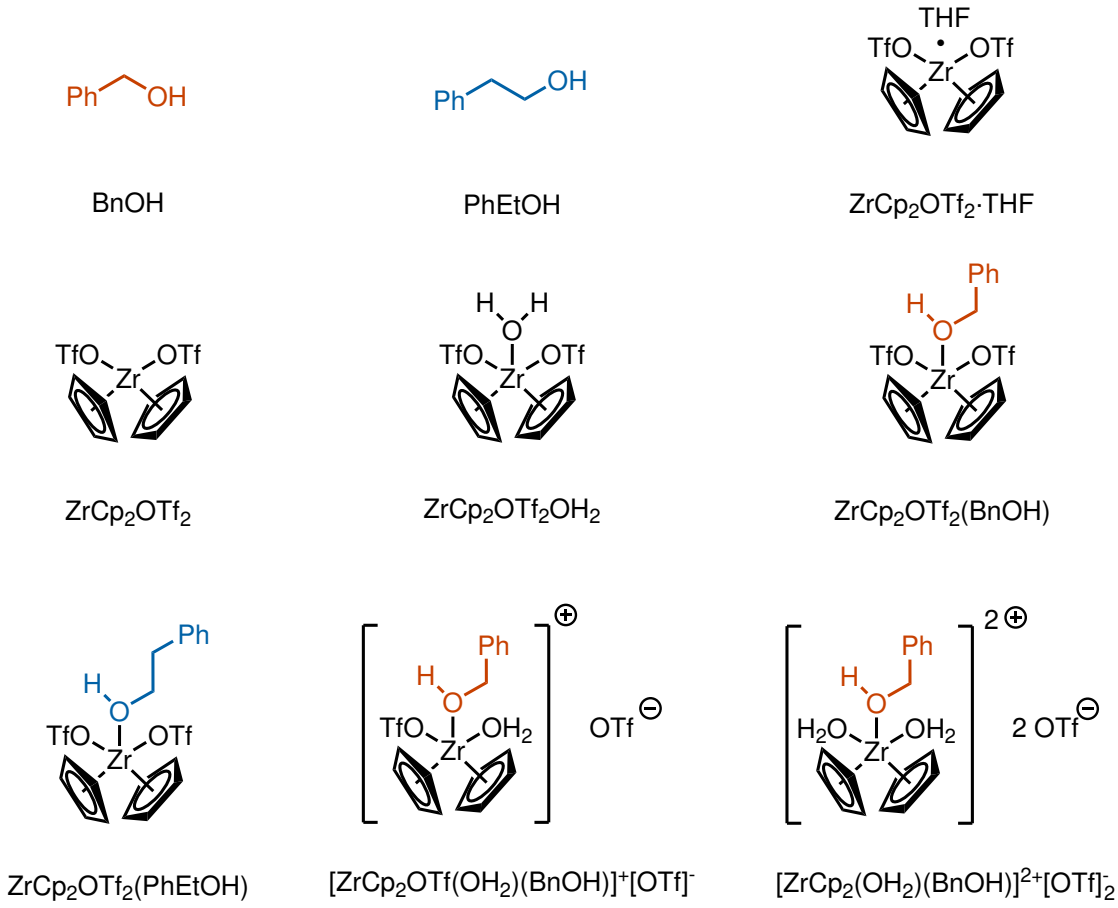

Figure 8: Lewis structures of the investigated species

The coordination of either BnOH or PhEtOH does not exert a significant impact on the formal partial charge of the oxygen atom within the studied molecules. While the NBO charges estimated the uncoordinated oxygen atom of BnOH or PhEtOH to be -0.76, the partial charge ranged from -0.76 to -0.79. Additionally, the charge on Zr is not substantially alter with the coordination. Specifically, while $ZrCp_2OTf_2$ exhibited a partial charge of 1.63 for Zr, the coordinated species with THF or BnOH/PhEtOH showed partial charges ranging from 1.51 to 1.53. Thus no clear electron transfer from Zr to O can be observed, which would indicate an activation of the alcohols. Zr-O bond distance for the Zr-Cp_2OTf_2(BnOH) and Zr-Cp_2OTf_2(PhEtOH) complexes show identical bond lengths, estimated at 2.295 Å. Substitution of the OTf ligands with H_2O led to a minor reduction in bond length, resulting in lengths of 2.260 Å and 2.267 Å, respectively. The differences in Gibbs free energies between the various species exhibit a more noticeable variation. $ZrCp_2OTf_2$(BnOH) exhibits a slight energy preference compared to $ZrCp_2OTf_2$(PhEtOH), with a $\Delta\Delta G$ of -0.2 kcal/mol. This suggests that a zirconocene species coordinated with BnOH is more favorable than with PhEtOH. Furthermore, the ligand exchange of OTf with H_2O in the $ZrCp_2OTf_2$(BnOH) complex results in a considerable energy cost. The exchange of one OTf ligand yields a $\Delta\Delta G$ of 8.3 kcal/mol, while the exchange of two OTf ligands leads to a $\Delta\Delta G$ of 15.7 kcal/mol. Also, $ZrCp_2OTf_2OH_2$ was identified as the most stable species, implying that it could potentially represent the resting state of the cat-

Compound	Bond distance [Å] Zr-O	Charge on Zr	Charge on O	ΔG [kcal/mol]
BnOH	-	-	-0.76	-
PhEtOH	-	-	-0.76	-
$ZrCp_2OTf_2 \cdot THF$	-	1.52	-	Reference (0.0)
$ZrCp_2OTf_2$	-	1.63	-	2.6
$ZrCp_2OTf_2OH_2$	2.237	1.49	-0.92	-2.6
$ZrCp_2OTf_2$(BnOH)	2.295	1.52	-0.77	-2.0
$ZrCp_2OTf_2$(PhEtOH)	2.295	1.51	-0.76	-1.8
$[ZrCp_2OTf(OH_2)(BnOH)]^+[OTf]^-$	2.260	1.53	-0.79	6.3
$[ZrCp_2(OH_2)_2(BnOH)]^+[OTf]_2^-$	2.267	1.53	-0.79	13.7

Table 2: Zr-O, with O representing the coordinated oxygen of the alcohol, bond lengths are given in Å for different potentially catalytic active species. Partial charges on Zr and O, the coordinated oxygen of the alcohol, were estimated using NBO analysis. The variation in ΔG regarding $ZrCp_2OTf_2 \cdot THF$ is given in kcal/mol. Level of theory: DLPNO-CCSD(T)-CPCM(toluene)/def2-TZVP//ωB97XD-CPCM(toluene)/def2-SVP.

alytic system. The heightened stability is likely attributed to the formation of two hydrogen bonds between water and the triflate ligands, whereas alcohols can only engage in the formation of a single hydrogen bond (see Figure 9). Furthermore, it's important to consider that alcohols have more steric hindrance than water, which also impacts stability. This influence can be observed through the differences in bond angles α and β, which represent the different fTO-Zr-OH_2 and fTO-Zr-OR bond angles (R stands for the rest of the alcohol). Notably, for $ZrCp_2OTf_2OH_2$, α and β have the same values (72.8°), whereas for $ZrCp_2OTf_2$(BnOH) (α=70.2°, β=72.3°) and $ZrCp_2OTf_2$(PhEtOH) (α=71.5°, β=71.8°), α and β are different.

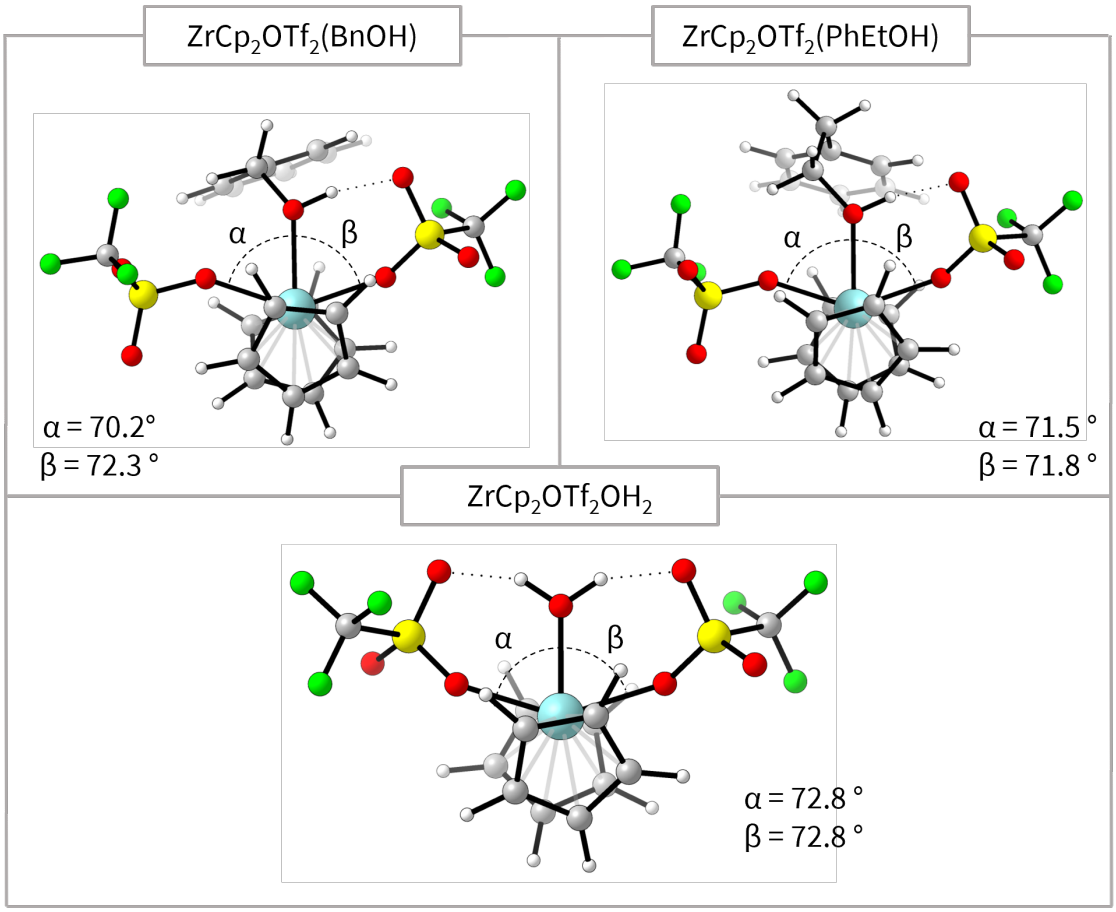

Figure 9: Molecular structure of $ZrCp_2OTf_2(BnOH)$ (top left), $ZrCp_2OTf_2(PhEtOH)$ (top right), and $ZrCp_2OTf_2OH_2$ (bottom middle). Angles are given in °. Atom colors: carbon (gray), hydrogen (white), fluorine (green), sulfur (yellow), zriconium (light blue), and oxygen (red).

To summarize all the preliminary findings before delving into a more in-depth mechanistic investigation, one can conclude:

1. Given that partial charges and bond distances remain unchanged when alcohols coordinate, it is unlikely that the zirconium catalyst is able to activate the alcohols.
2. The exchange of OTf ligands with water is associated with a high energetic cost, and as such, not further considered.
3. $ZrCp_2OTf_2OH_2$ is the most stable species among those considered, and therefore, it is likely the resting state of the catalytic cycle.

7.3 S_N2-like mechanism with $ZrCp_2OTf_2 \cdot THF$ as a catalyst

7.3.1 General idea behind an S_N2-like reaction with $ZrCp_2OTf_2 \cdot THF$ as acatalyst

Since the reaction is modeled in toluene (a nonpolar solvent) the initial investigation focused on an S_N2-like mechanism. Considering that a carbocation, which would be formed in an S_N1-like reaction, would not be effectively stabilized through solvation in such nonpolar environment, exploring the S_N2-like pathway was prioritized. This choice is further supported by experimental and computational studies on aluminum triflate, which suggest an S_N2-like mechanism for the direct substitution of alcohols in toluene.[56] In Figure 10, the proposed hypothetical catalytic cycle is visualized.

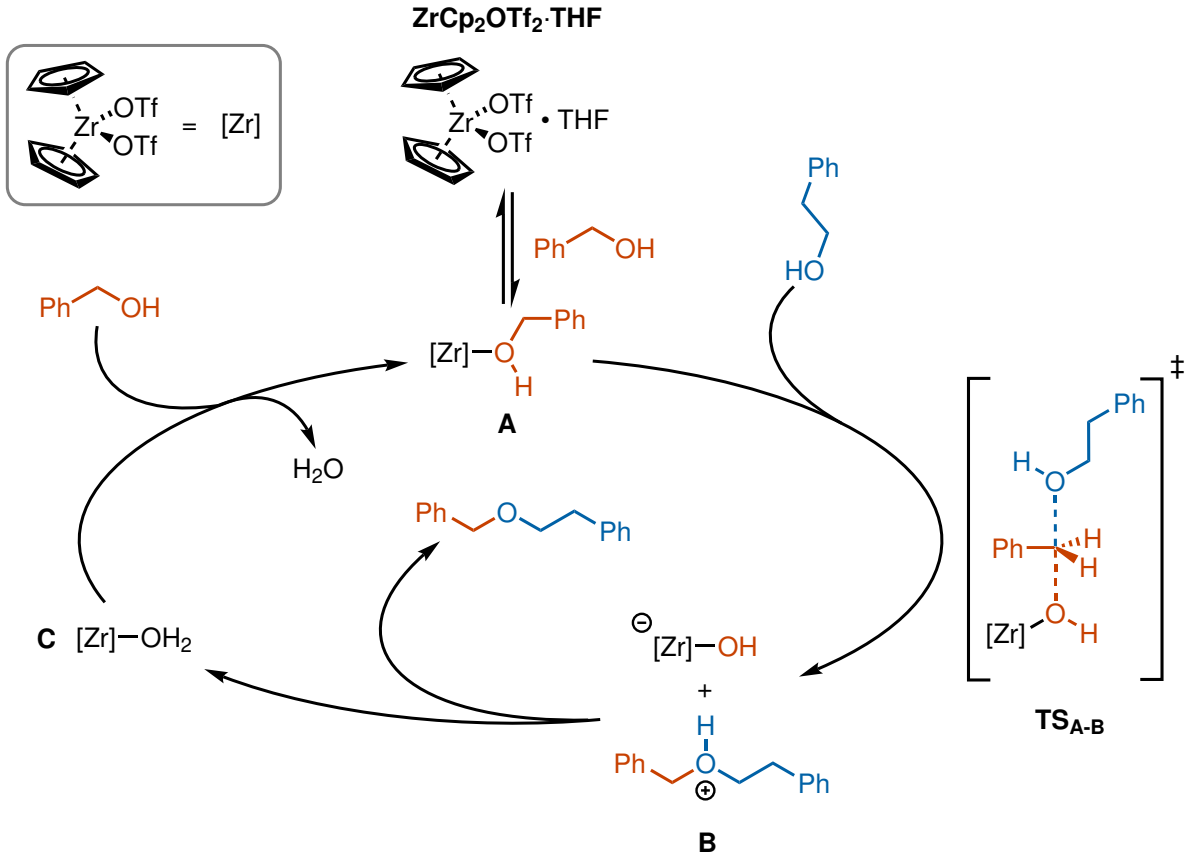

Figure 10: Proposed catalytic cycle for an S_N2-like mechanism.

The proposed mechanism would begin with a ligand substitution of THF with benzyl alcohol (**$ZrCp_2OTf_2 \cdot THF$→A**), followed by a nucleophilic attack of phenylethanol in an S_N2 style (**A→B**). Subsequently, reprotonation of the catalyst and release of the asymmetric ether would occur (**B→C**). To complete the catalytic cycle, a ligand substitution of water with benzyl alcohol takes place (**C→A**).

7.3.2 Computational investigation of an S_N2-like mechanism with $ZrCp_2OTf_2 \cdot THF$ as a catalyst

The energy profile of the S_N2-like reaction is illustrated in Figure 11, encompassing the formation of both the associated reactants and products. Moreover, the computed molecular structure of the $\mathbf{TS_{A\text{-}B,no\text{-}water}}$ is shown in Figure 13 **a**. When not considering the presence of water, a reaction barrier of $\Delta G^{\ddagger}(\mathbf{A_{no\text{-}water}} \rightarrow \mathbf{B_{no\text{-}water}})$ = 36.6 kcal/mol was determined (see Figure 11). Despite the elevated reaction temperatures (100 °C), the barrier remains beyond an energetically accessible range. However, recognizing that water is an essential component of the reaction, a more in-depth investigation was undertaken to evaluate its potential role in reducing the reaction barrier.
Subsequently, microsolvation was employed through the introduction of water molecules to the system to examine their effect on the barrier (see Figure 11). However, introduction of a single water molecule did not result in a decrease of the energy barrier; rather, it led to an increase in the barrier ($\Delta G^{\ddagger}(\mathbf{A_{one\text{-}water}} \rightarrow \mathbf{B_{one\text{-}water}})$ = 44.6 kcal/mol), propably due to the increased entropic energy of the system. Also, TS molecular geometries showed some noticeable differences. For example, Atom distances between C and O atoms which are form and break bonds during the TS are slightly elongated in $\mathbf{TS_{A\text{-}B,no\text{-}water}}$ compared to $\mathbf{TS_{A\text{-}B,one\text{-}water}}$ (see Figure 13 **a** and **b**). More significant then the stretched bond lengths in the TS geometry are the differences in the bond angles. In the absence of water interactions, the C-O-C bond angle measures 159.9°, while the presence of one water molecule leads to a more constrained angle of 151.1°. These geometric changes could significantly impact the energetic barrier, primarily due to steric hindrance and repulsion effects between the water molecule and the hydrophobic aryl moiety of the alcohols.
Continuing the investigation of the role of water during the reaction, additional water molecules were introduced. The arrangement of these water molecules forms a distinctive chain-like structure, which in turn facilitates a direct proton transfer. This exceptional configuration not only enables the direct formation of the ether but also accomplishes the concurrent regeneration of the catalyst in a single, integrated step. Despite the fact that TS geometries exhibited greater structural resemblance to $\mathbf{TS_{A\text{-}B,no\text{-}water}}$ as opposed to $\mathbf{TS_{A\text{-}B,one\text{-}water}}$, (see Figure 13), the energetic barriers remained elevated. The energetic profile of the reaction is shown in Figure 12. While in the presence of two water molecules marginally lowered the estimated reaction barrier about 0.2 kcal/mol compared to the presence of only one water molecule ($\Delta G^{\ddagger}(\mathbf{A_{two\text{-}water}} \rightarrow \mathbf{C_{two\text{-}water}})$ = 44.4 kcal/mol), it remained still 7.8 kcal higher compared to reaction with no water present. Further addition of water to the system increased the reaction barrier up to 10.5 kcal/mol ($\Delta G^{\ddagger}(\mathbf{A_{three\text{-}water}} \rightarrow \mathbf{C_{three\text{-}water}})$ = 47.1 kcal/mol).

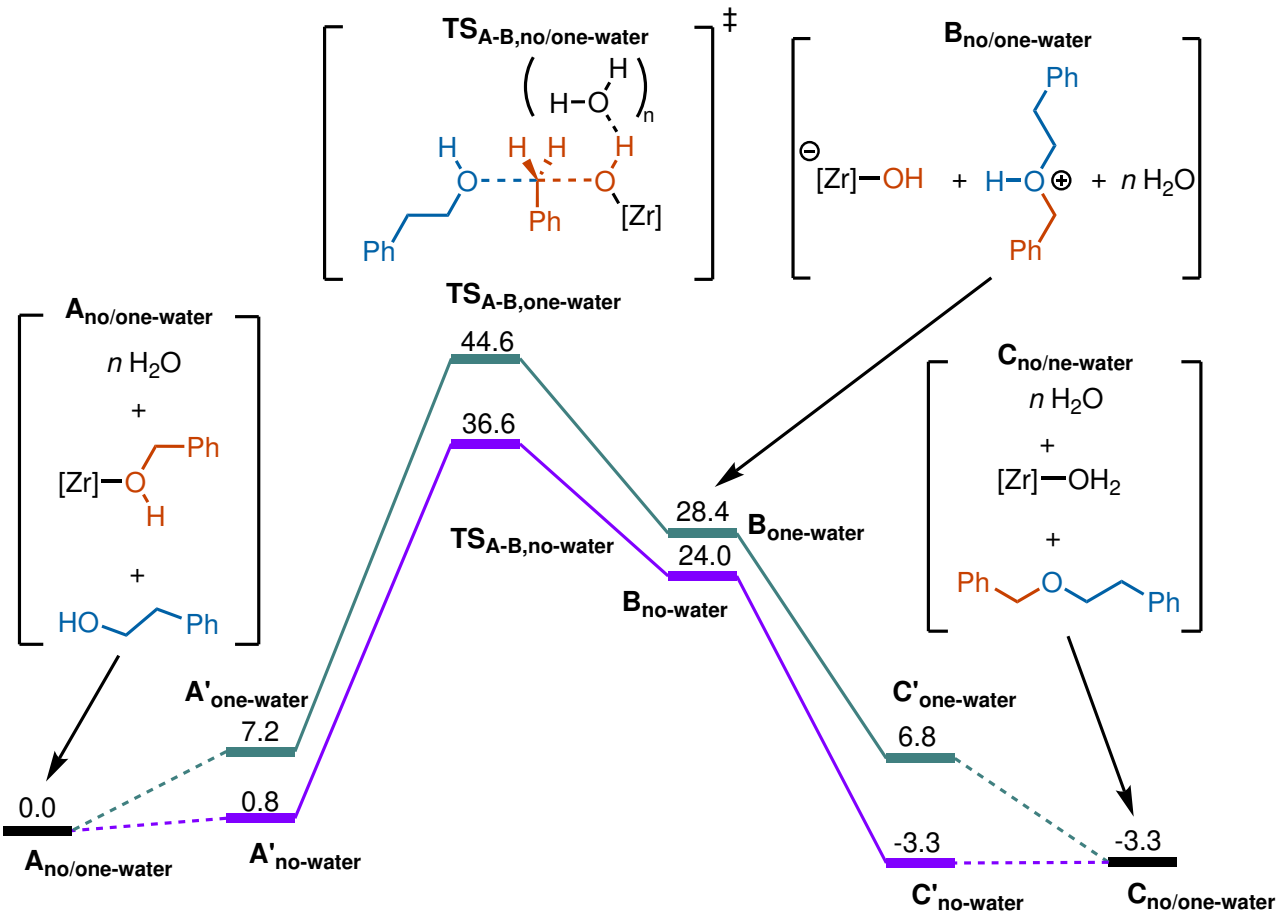

Figure 11: Energy profile (relative Gibbs free energies($\Delta G_{373\,K,\,toluene}$ [kcal/mol]) of S_N2-like reaction with no water (purple) and with one water molecule (green). Reactant and product complexes are labeled with an apostrophe. The sum of the reactant energies is taken as a reference (0.0 kcal/mol). n = 0 or 1. Level of theory: DLPNO-CCSD(T)-CPCM(toluene)/def2-TZVP//ωB97XD-CPCM(toluene)/def2-SVP.

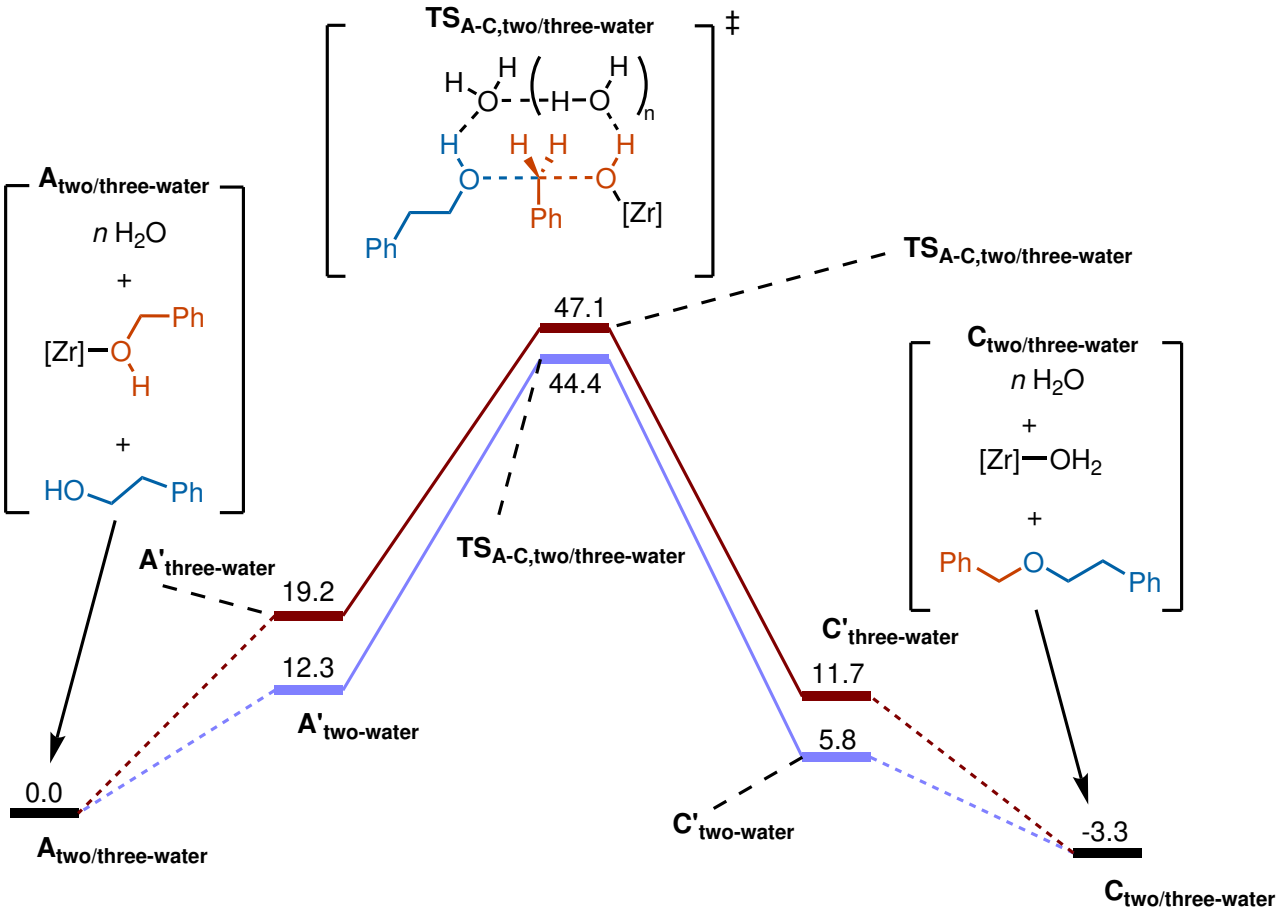

Figure 12: Energy profile (relative Gibbs free energies($\Delta G_{373\,K,\,toluene}$ [kcal/mol]) of S_N2-like reaction with two water molecules (lilac) and with three molecules (brown). Reactant and product complexes are labeled with an apostrophe. The sum of the reactant energies is taken as a reference (0.0 kcal/mol). n = 2 or 3. Level of theory: DLPNO-CCSD(T)-CPCM(toluene)/def2-TZVP//ωB97XD-CPCM(toluene)/def2-SVP.

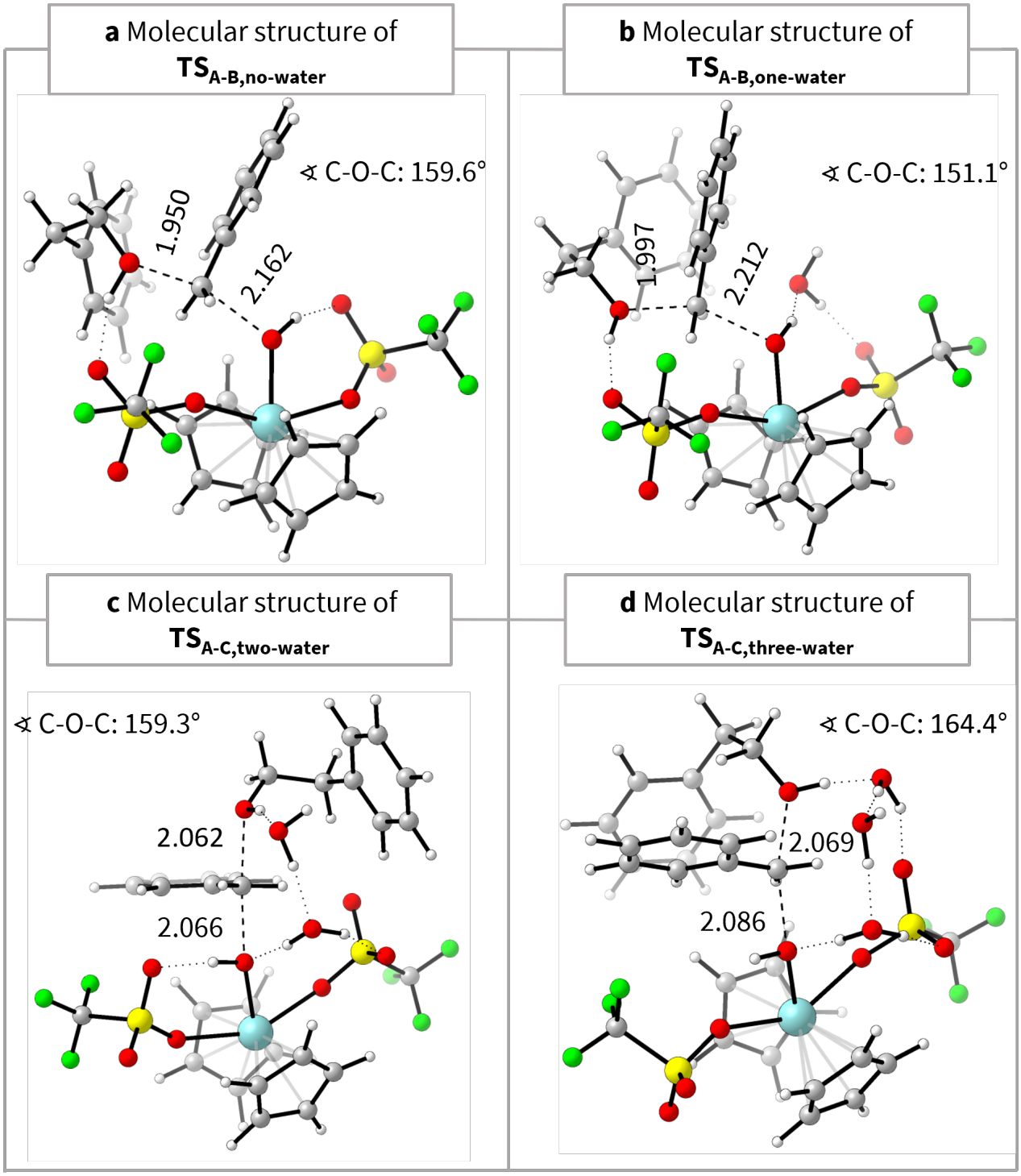

Figure 13: Molecular structure of the TS of the S_N2-like reaction with no water (**$TS_{A\text{-}B,no\text{-}water}$**) (**a**), one water molecule (**$TS_{A\text{-}B,one\text{-}water}$**) (**b**), two water molecules (**$TS_{A\text{-}C,two\text{-}water}$**) (**c**), and three water molecules (**$TS_{A\text{-}C,three\text{-}water}$**) (**d**). Atom colors: carbon (gray), hydrogen (white) , fluorine (green), sulfur (yellow), zriconium (light blue), and oxygen (red). Distances shown in Å and angles in °.

In addition to $ZrCp_2OTf_2$(BnOH) (**A**) serving as the initial species of the catalytic cycle, $ZrCp_2OTf_2$(PhEtOH) ($\mathbf{A_i}$) was also considered as starting point of the reaction. The corresponding energy profile is displayed in Figure 14.

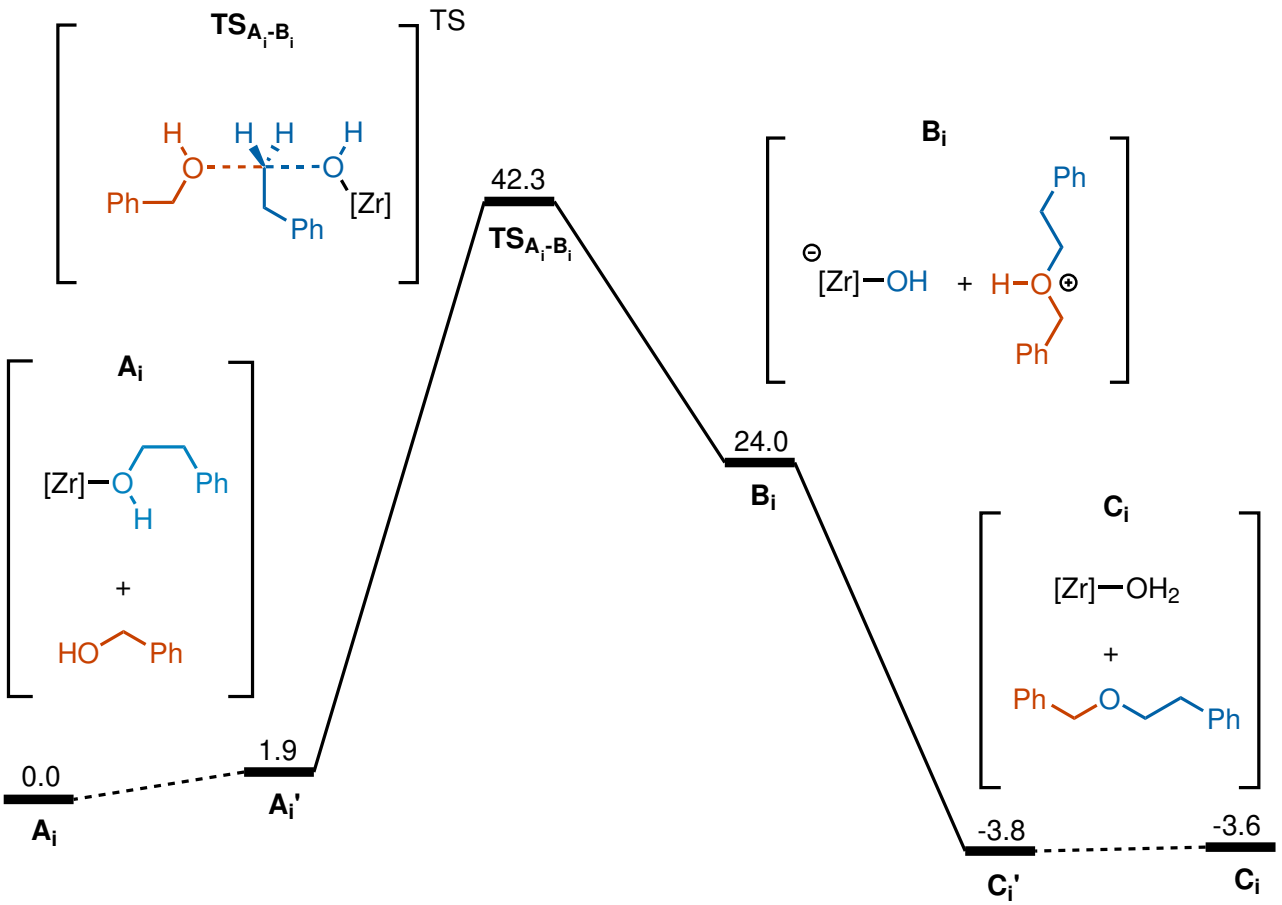

Figure 14: Energy profile (relative Gibbs free energies($\Delta G_{373\,K,\,toluene}$ [kcal/mol]) of an S_N2-like reaction with BnOH as nucleophile. Reactant and product complexes are labeled with an apostrophe. The sum of the reactant energies is taken as a reference (0.0 kcal/mol). Level of theory: DLPNO-CCSD(T)-CPCM(toluene)/def2-TZVP//ωB97XD-CPCM(toluene)/def2-SVP.

As expected, the reaction barrier for $\mathbf{A_i}$→$\mathbf{B_i}$ ($\Delta G^{\ddagger}$ = 42.3 kcal/mol) is higher compared to $\mathbf{A_{no\text{-}water}}$→$\mathbf{B_{no\text{-}water}}$ ($\Delta G^{\ddagger}$ = 36.6 kcal/mol). This difference is likely attributed to the fact that the CH_2 group of BnOH is more electrophilic when contrasted with the CH_2 group of PhEtOH, due to the proximity of the phenyl moiety. In other words, when BnOH is used, the conjugation of the aryl ring stabilizes the transition state (TS) during a nucleophilic attack. However, when an additional CH_2 group is present like in PhEtOH, the TS cannot be stabilized through conjugation.
In conclusion, for the studied catalyst, an S_N2-like pathway is inaccessible due to the high energetic barrier. Furthermore, the introduction of water into the system did not lower the energetic barrier of the reaction; in fact, led to an even higher barrier.

7.4 S_N1-like mechanism with $ZrCp_2OTf_2 \cdot THF$ as a catalyst

7.4.1 General idea behind an S_N1-like reaction with $ZrCp_2OTf_2 \cdot THF$ as a catalyst

Intrigued by preceding experimental findings related to Hf, La, Yb, and Sc triflates, which suggest an S_N1-like mechanism, this pathway was also explored in the present theoretical study. However, the substrate scope of these triftlates is limited to secondary benzylic alcohols,[57, 58] while $ZrCp_2OTf_2 \cdot THF$ is capable to transform primary benzylic alcohols. Findings of the Lundberg and coworkers have disclosed that the reaction of PhEtOH and (*S*)-1-phenylethanol led to the racemization of the ether product, providing evidence for a mechanism involving a carbocationic intermediate (see Figure 15).[10]

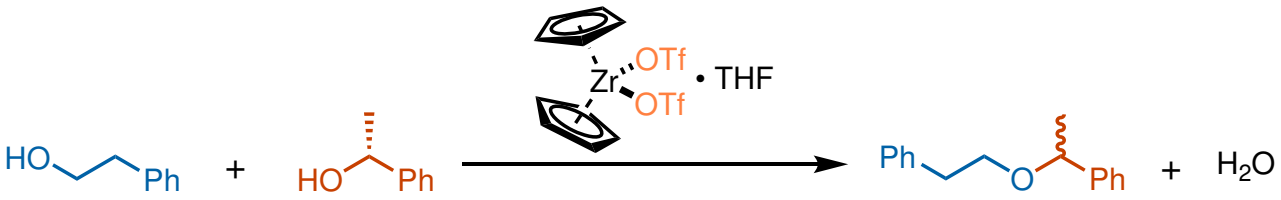

Figure 15: Racemization of (*S*)-1-phenylethanol in the etherification reaction.

A hypothetical S_N1-like mechanism is visualized in Figure 16. After, the ligand substitution of THF with benzyl alcohol (**$ZrCp_2OTf_2 \cdot THF$→A**), a benzylic carbocation would be formed (**A→D**). Subsequently, the second alcohol can attack either face of the planar carbocation (**D→B**). The formed protonated ether can then reprotonaed the catalyst (**B→C**). Substitution of water with benzyl alcohol would close the catalytic cycle (**C→A**).

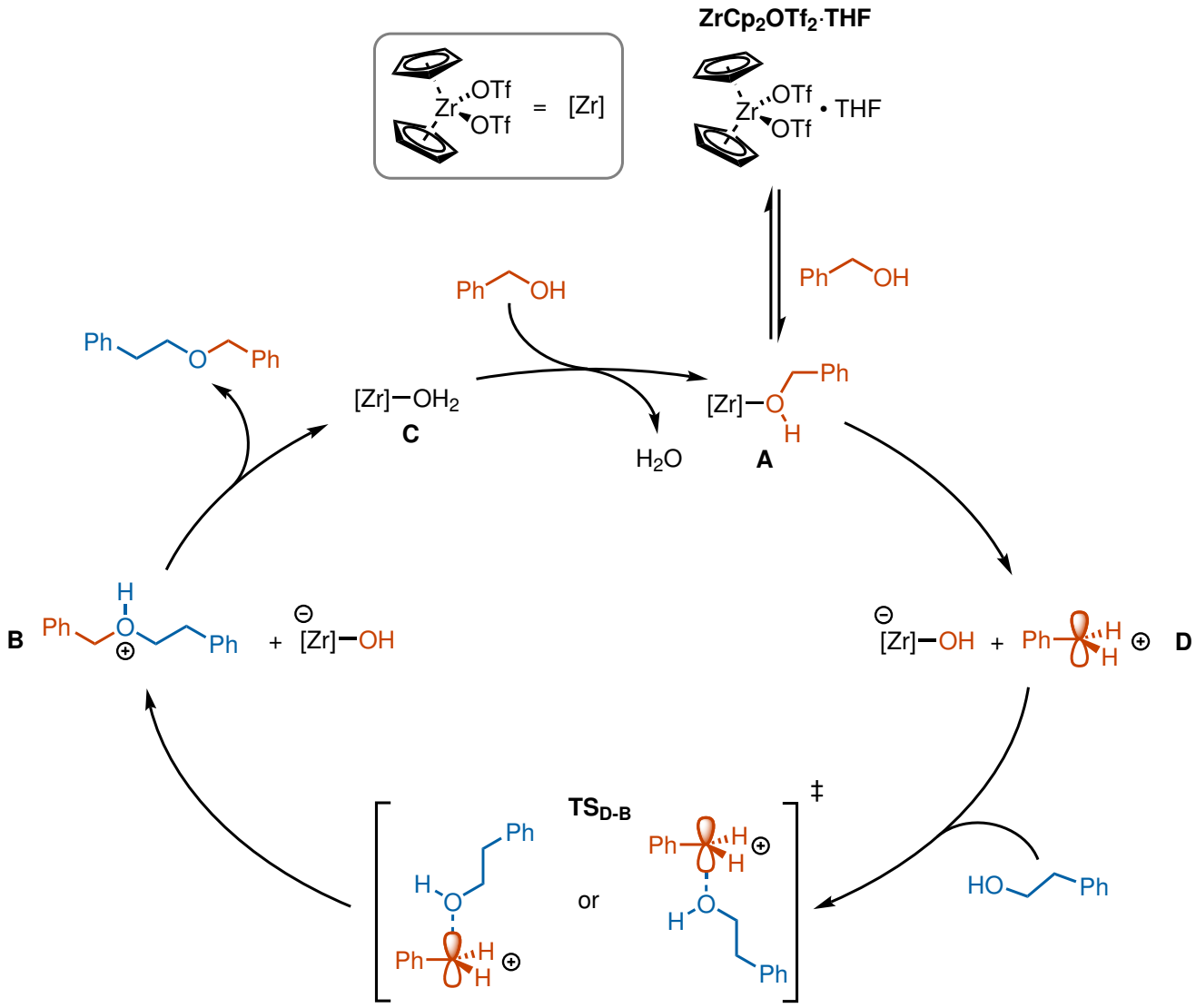

Figure 16: Proposed catalytic cycle for an S_N1-like mechanism.

7.4.2 Computational investigation of an S_N1-like mechanism with $ZrCp_2OTf_2 \cdot THF$ as a catalyst

The energy profile of the formation of a carbocation in an S_N1-like reaction is displayed in Figure 17. The computed energetic barrier was found to be surprisingly high, despite the expected resonance stabilization of the formed benzyl cation ($\Delta G^{\ddagger}$(**A**→**D**) = 47.4 kcal/mol). These results highlight that an S_N1-like pathway is not feasible under the given conditions.

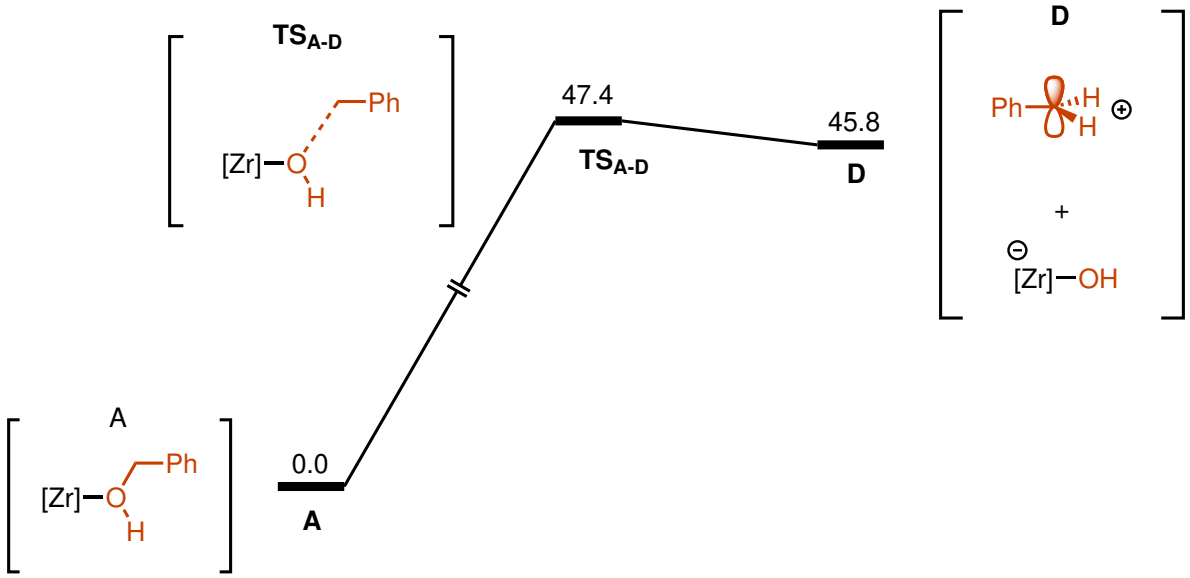

Figure 17: Energy profile (relative Gibbs free energies ($\Delta G_{373\,K,\,toluene}$ [kcal/mol]) of the formation of a benzyl carbocation catalyzed by the zirconocene complex. The sum of the reactant energies is taken as a reference (0.0 kcal/mol). Level of theory: DLPNO-CCSD(T)-CPCM(toluene)/def2-TZVP//ωB97XD-CPCM(toluene)/def2-SVP

.

However, due to the high reaction barrier found for carbocation formation, the subsequent reaction to close the catalytic cycle (**D**→**A**), which involves the attack of a second alcohol, was not investigated more closely.

In summary, an S_N1-like reaction is even more energetically unfavorable than an S_N2-like reaction catalyzed by $ZrCp_2OTf_2 \cdot THF$. The experimental findings of the Lundberg group could be attributed to the fact that the substrate, a secondary benzyl alcohol, is more prone to forming a carbocation due to the stabilizing influence of the additional methyl group.

7.5 Formation of a Bn-OTf species by $ZrCp_2OTf_2 \cdot THF$

7.5.1 General idea behind the Bn-OTf formation with $ZrCp_2OTf_2 \cdot THF$

In order to identify a TS for carbocation formation, a relaxed potential energy surface (PES) scan was performed. To achieve this, the C-O bond was intentionally elongated. Surprisingly, instead of forming a carbocation, the elongation led to the creation of a new C-O bond within the OTf moiety. Building upon this discovery that an $ZrCp_2(OTf)(OH) \cdot$(Bn-OTf) (**E**) appears to be preferred over the formation of a carbocation, a proposed catalytic cycle is visualized in Figure 18.

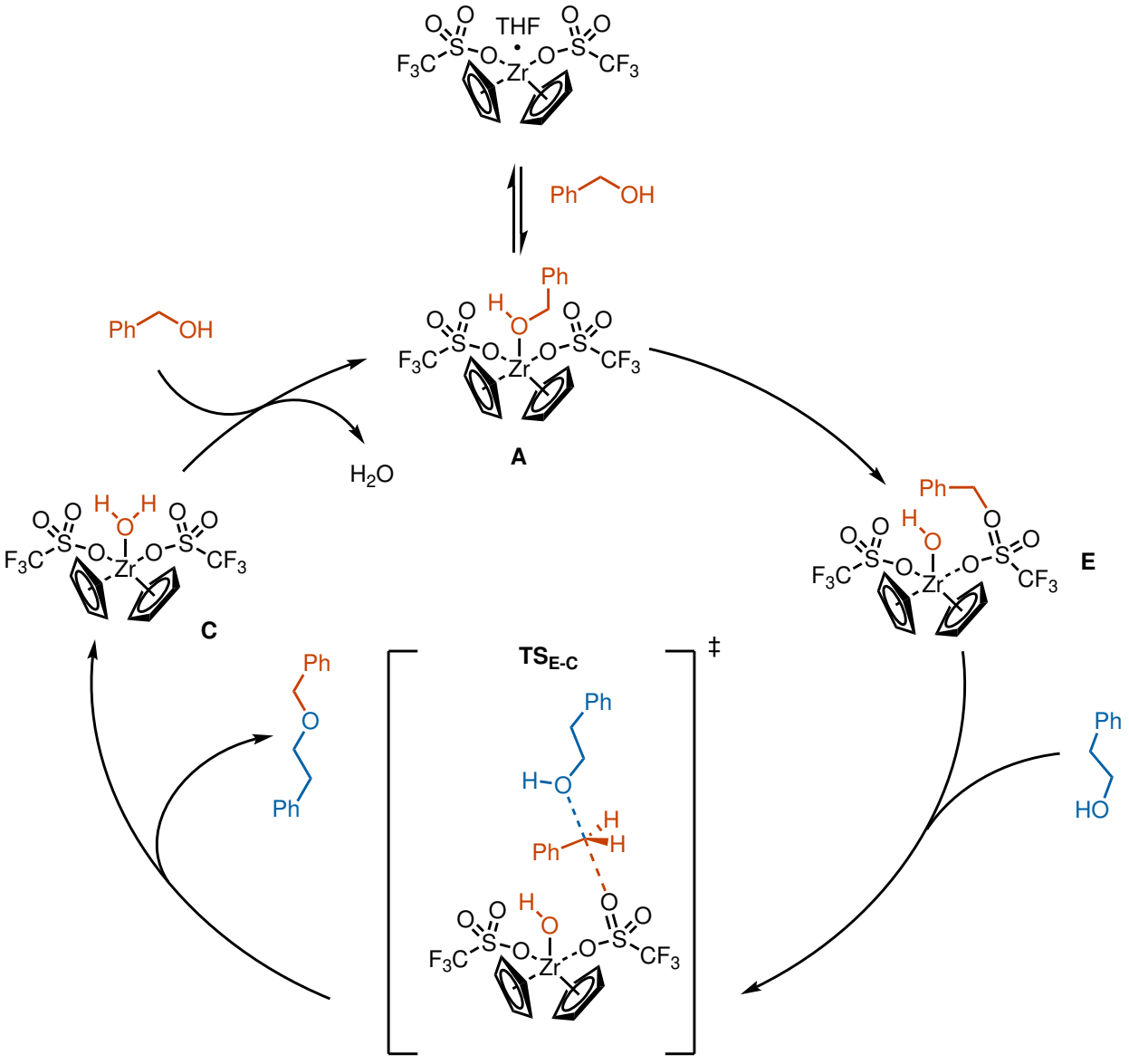

Figure 18: Proposed catalytic cycle for the formation of activated Bn-OTf (**E**)followed by a nucleophilic attack of PhEtOH.

The proposed catalytic cycle commences with the ligand substitution of THF with benzyl alcohol (**$ZrCp_2OTf_2 \cdot THF$→A**). This is followed by the creation of BnOTf which is coordinated to the zirconocene complex (**A→E**). Subsequently, PhEtOH can attack species **E** (**E→C**) to form the asymmet-

ric ether. Finally, ligand substitution of water with benzyl alcohol takes place, completing the catalytic cycle (**C**→**A**).

The energy profile for the entire reaction is illustrated in Figure 19. As anticipated by PES scan, the the formation of species **E** is prefered over the generation of a carbocation. However, the energy barrier remains relatively high ($\Delta G^{\ddagger}$(**A**→**E**) = 44.7 kcal/mol). This considerable barrier strongly suggests the unlikelihood of this mechanistic pathway. The molecular structure of the transition state (TS) is shown in Figure 20 **a**, while the structure of the formed species **E** is presented in Figure 20 **b**. The determined Zr-O bond length in the coordinated BnOTF species is significantly elongated (0.441 Å) in comparison to the unsubstituted OTf group. This observation suggests that the BnOTF moiety is only weakly coordinated to the metal complex.

For the subsequent nucleophilic attack of PhEtOH on **E**, similar to the previously studied S_N2-like reaction (see subsubsection 7.3.2), the impact of water was investigated. In contrast to the S_N2-like reaction discussed in subsubsection 7.3.2, the nucleophilic attack of PhEtOH on **E** and reprotonation occur simultaneously, even in the absence of water. The transition state geometry (see Figure 20 **c**), which inherently allows for both processes to take place in a single step. Nonetheless, water was placed to see if it could lower the reaction barrier. However, the presence of water did not have a positive impact on the reaction; instead, it resulted in an increase in the barrier by 2.0 kcal/mol compared to when no water was present ($\Delta G^{\ddagger}$(**E**$_{\textbf{no-water}}$→**C**$_{\textbf{no-water}}$ = 23.7 kcal/mol, $\Delta G^{\ddagger}$(**E**$_{\textbf{one-water}}$→**C**$_{\textbf{one-water}}$) = 25.7 kcal/mol). The molecular structures of the TS are shown in Figure 20 **d**. Interestingly, the presence of water has only a minor impact on the C-O bond distances, with differences of less than 0.03 Å. However, the C-O-C angle widens by 6.7° when water is introduced.

Considering these results, one can conclude that the formation of BnOTF through the attack of BnOH onto an OTf ligand is slightly more favorable than the formation of the carbocation. Nevertheless, both processes remain unlikely to occur due to the high energetic barrier. However, these results demonstrate that BnOTF can readily participate in a reaction to form an ether.

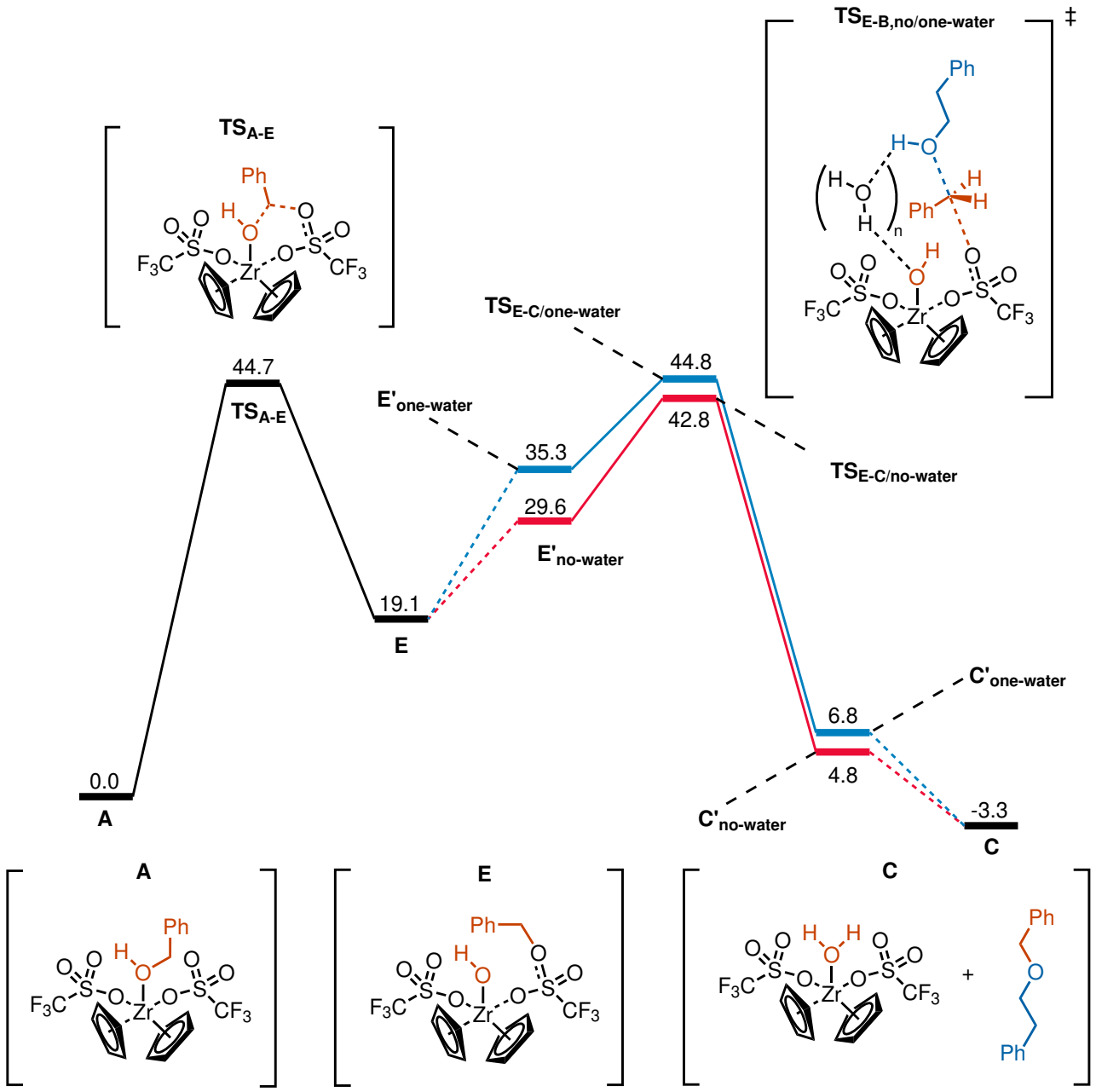

Figure 19: Energy profile (relative Gibbs free energies($\Delta G_{373\,K,\,toluene}$ [kcal/mol]) for the formation of **E** (black), followed by a nucleophilic attack of PhEtOH with no water molecules present (red), and one no water molecule present (blue). Reactant and product complexes are labeled with an apostrophe. The sum of the reactant energies is taken as a reference (0.0 kcal/mol). Level of theory: DLPNO-CCSD(T)-CPCM(toluene)/def2-TZVP//ωB97XD-CPCM(toluene)/def2-SVP.

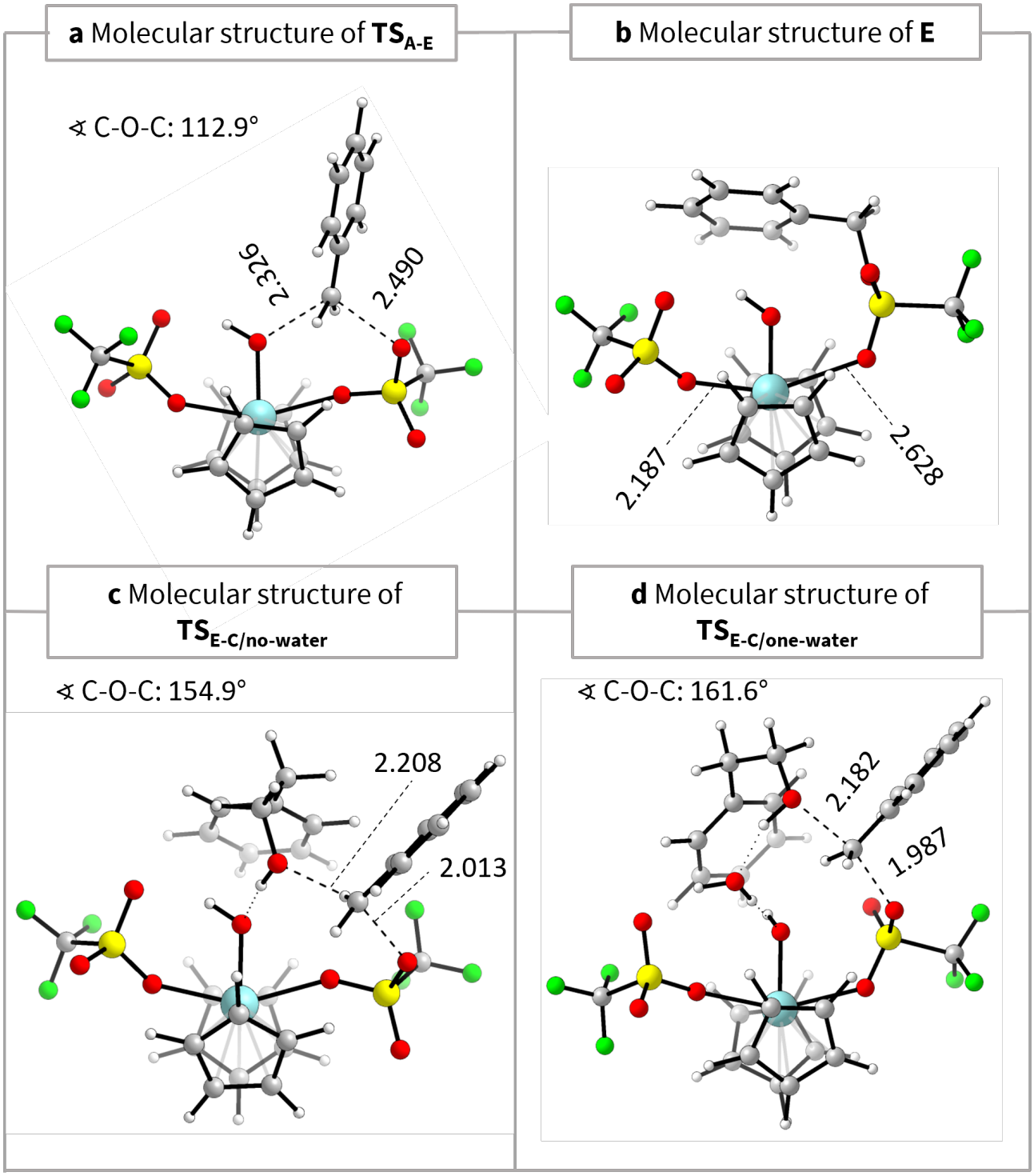

Figure 20: Molecular structure of **TS$_{A-E}$** (**a**), **E** (**b**), **TS$_{E-C/nowater}$** (**c**), and **TS$_{E-C/onewater}$** (**d**). Atom colors: carbon (gray), hydrogen (white) , fluorine (green), sulfur (yellow), zriconium (light blue), and oxygen(red). Distances shown in Å and angles in °.

7.6 $ZrCp_2OTf_2 \cdot THF$ as a Brønsted acid catalyst

Furthermore, it was investigated if $ZrCp_2OTf_2 \cdot THF$ can function as a Brønsted acid after a replacement of THF with a water molecule. In this proposed catalytic cycle (Figure 21), the process is initiated with hydrolysis, involving the replacement of the THF ligand with water. The resulting species (**C**) would then protonate BnOH. Subsequently, the formed species (**F**) could be attacked by PhEtOH. Probably the protonated asymmetric ether (**B**) could then protonate the zirconocene complex to regenerate the catalyst (**C**).

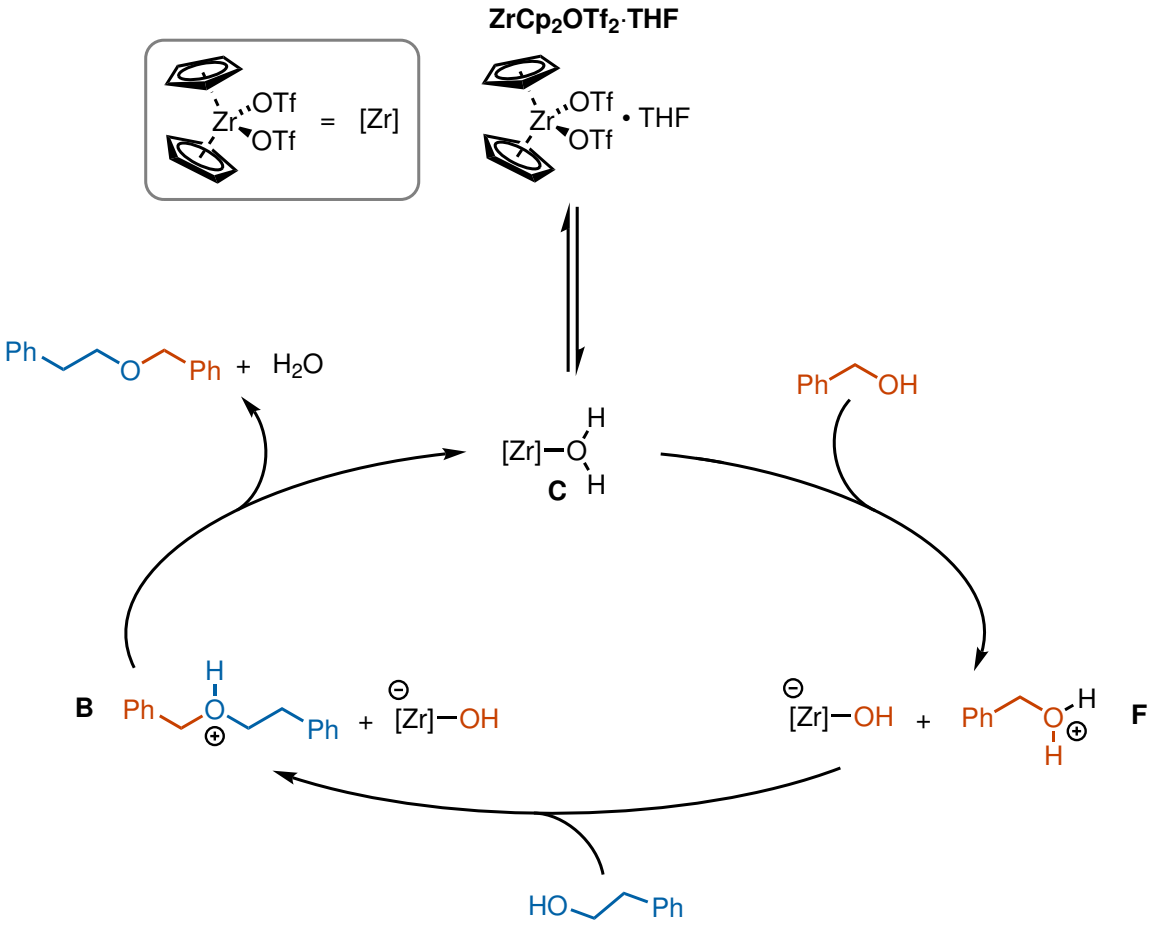

Figure 21: Proposed catalytic cycle in which $ZrCp_2OTf_2OH_2$ serves as a Brønsted acid to catalyze the reaction in an S_N2-like manner.

The energy profile for the described reaction is depicted in Figure Figure 22. In addition to the primary protonation of BnOH, the protonation of PhEtOH was also investigated to compare the two possible pathways. For the protonation of BnOH and the nucleophilic attack of PhEtOH a barrier of $\Delta G^{\ddagger}$(**C**→**B**) = 44.7 kcal/mol was found. This barrier is 4.4 kcal/mol lower ($\Delta G^{\ddagger}$(**C**→**C$_i$-B$_i$**) = 49.1 kcal/mol), compared to inversed reaction, where the protonated alcohol PhEtOH gets attacked by BnOH. Nonetheless, both barriers do not fall within a range that is achievable under the applied reaction conditions.

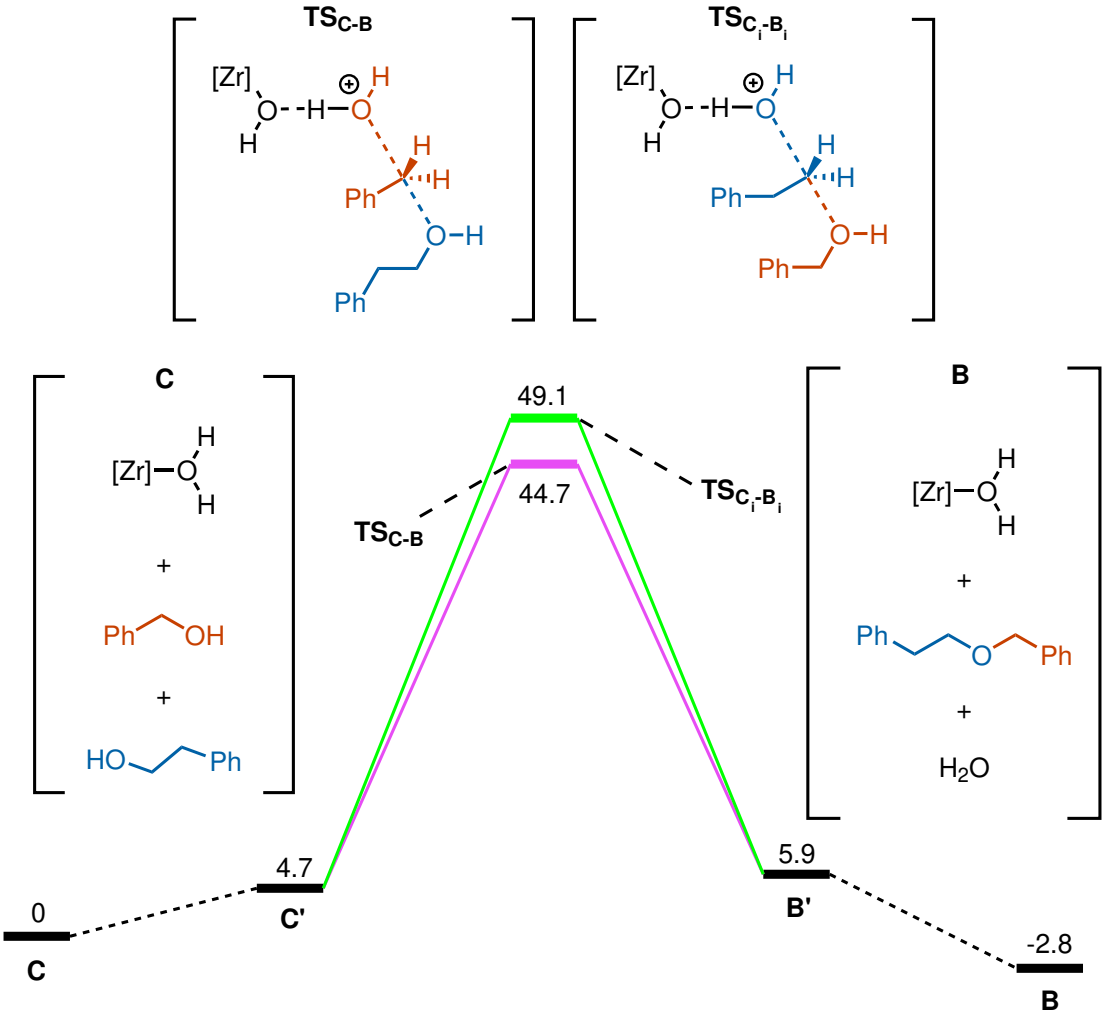

Figure 22: Energy profile (relative Gibbs free energies($\Delta G_{373\,K,\,toluene}$ [kcal/mol]) for a nucleophilic attack of PhEtOH after protonation of BnOH by $ZrCp_2OTf_2OH_2$ (pink), and vice versa (green; nucleophilic attack of BnOH after protonation of PhEtOH by $ZrCp_2OTf_2OH_2$. Reactant and product complexes are labeled with an apostrophe. The sum of the reactant energies is taken as a reference (0.0 kcal/mol). Level of theory: DLPNO-CCSD(T)-CPCM(toluene)/def2-TZVP//ωB97XD-CPCM(toluene)/def2-SVP.

7.7 $ZrCp_2OTf_2 \cdot THF$ as a precatalyst which can form HOTf

Another potential mechanism was explored in which $ZrCp_2OTf_2OH_2$ acts as a precatalyst. This investigation was motivated by reports indicating that many metal triflates can readily undergo hydrolysis reactions, leading to the release of HOTf.[59]

7.7.1 S_N2-like reaction catalyzed by HOTf

Firstly, an S_N2-like reaction was explored. A potential reaction mechanism is depicted in Figure 23. In the proposed mechanism, **$ZrCp_2OTf_2 \cdot THF$** would react with water to produce HOTf (**G**), which could then protonate BnOH (**G**→**H**), thus activating the alcohol for a nucleophilic attack by PhEtOH (**H**→**I**). Following the nucleophilic attack, the resulting protonated ether could subsequently reprotonate the OTf anion to regenerate HOTf (**I**→**G**).

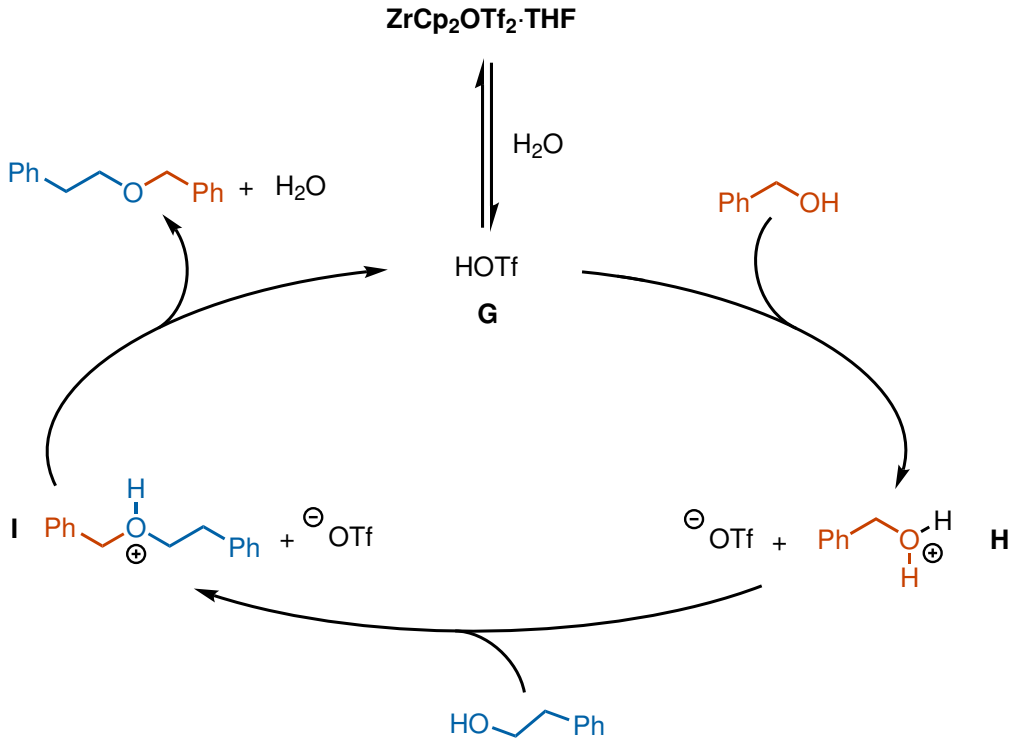

Figure 23: Proposed catalytic cycle in which $ZrCp_2OTf_2 \cdot THF$ serves as a precatalyst, releasing HOTf, which then act as a Brønsted acid to catalyze the reaction in an S_N2-like manner.

The energy profile for the described reaction is depicted in Figure 24 (maroon). A barrier of $\Delta G^{\ddagger}$(**G**→**I**) = 28.4 kcal/mol was determined. Since this barrier falls within a feasible range, the reaction was further investigated by reversing the roles of the attacking and protonated alcohols. Protonating PhEtOH and then having BnOH attack raised the barrier as expected, by 5.4 kcal/mol compared to the reverse reaction ($\Delta G^{\ddagger}$(**G**→**I**$_i$) = 33.6 kcal/mol), as shown in Figure 24 (olive).
The formation of symmetric ethers was also explored. Protonation of BnOH followed by the attack of another BnOH molecule resulted in almost the same energetic barrier ($\Delta G^{\ddagger}$(**J**→**K**) = 29.0 kcal/mol, see Figure 25 turquoise) when compared to PhEtOH attacking the protonated BnOH

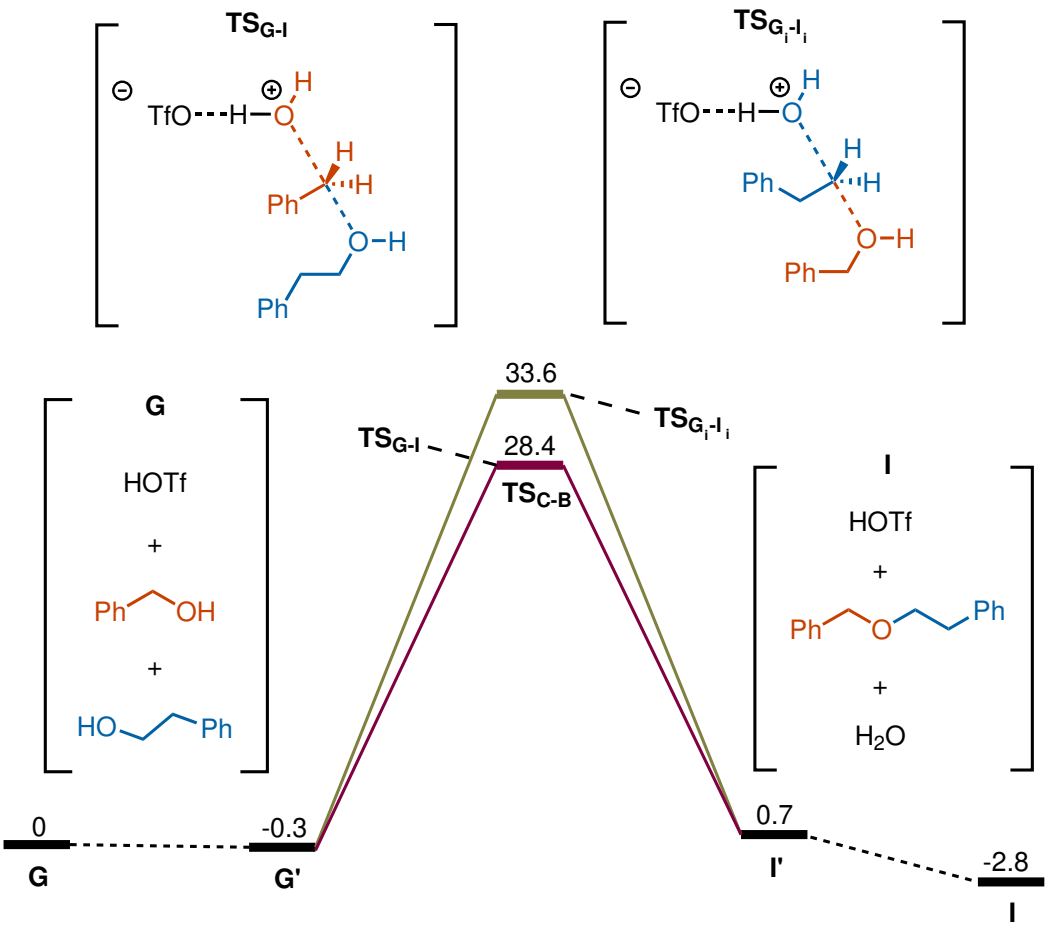

Figure 24: Energy profile (relative Gibbs free energies ($\Delta G_{373\,K,\,toluene}$ [kcal/mol]) for a nucleophilic attack of PhEtOH after protonation of BnOH by HOTf (maroon), and vice versa (olive; nucleophilic attack of BnOH after protonation of PhEtOH by HOTf). Reactant and product complexes are labeled with an apostrophe. The sum of the reactant energies is taken as a reference (0.0 kcal/mol). Level of theory: DLPNO-CCSD(T)-CPCM(toluene)/def2-TZVP//ωB97XD-CPCM(toluene)/def2-SVP.

species ($\Delta\Delta G^{\ddagger}$ = 0.6 kcal/mol). As expected, protonation of PhEtOH followed by the attack of another PhEtOH molecule notably increases the barrier ($\Delta G^{\ddagger}$(**L**→**M**) = 35.7 kcal/mol, see Figure 25 orange). The obtained results are consistent with experimental findings that diphenylethyl ether (PhEt-O-PhEt) is not observed as a reaction product, but rather the formation of dibenzyl ether (Bn-O-Bn) and the asymmetric ether (Bn-O-PhEt).

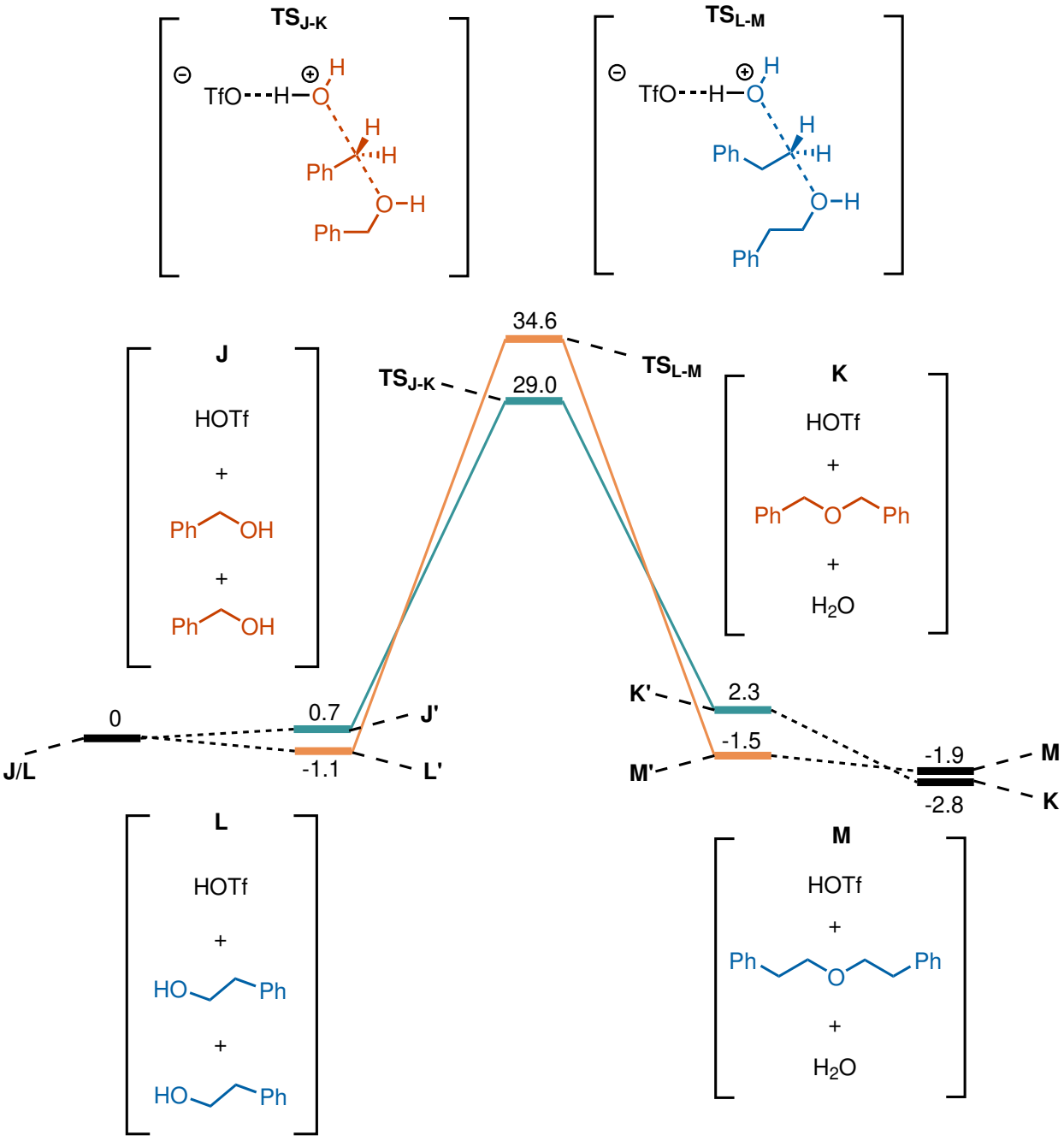

Figure 25: Energy profile (relative Gibbs free energies ($\Delta G_{373\,K,\,toluene}$ [kcal/mol]) for a nucleophilic attack of PhEtOH after protonation of another PhEtOH molecule by HOTf (orange), and nucleophilic attack of BnOH after protonation of another BnOH molecule by HOTf (turquoise). Reactant and product complexes are labeled with an apostrophe. The sum of the reactant energies is taken as a reference (0.0 kcal/mol). Level of theory: DLPNO-CCSD(T)-CPCM(toluene)/def2-TZVP//ωB97XD-CPCM(toluene)/def2-SVP.

7.7.2 S_N1-like reaction catalyzed by HOTf

In addition to investigating an S_N2-like mechanism, the possibility of an Brønsted acid initiated S_N1-like mechanism was also studied. However, similar to the previous investigation in subsubsection 7.4.2, when performing a PES scan to obtain the transition state for carbocation formation, the formation of a triflate species was observed instead of the carbocation. Therefore, an alternative mechanism (see Figure 26) was proposed instead of the direct formation of a carbocation.

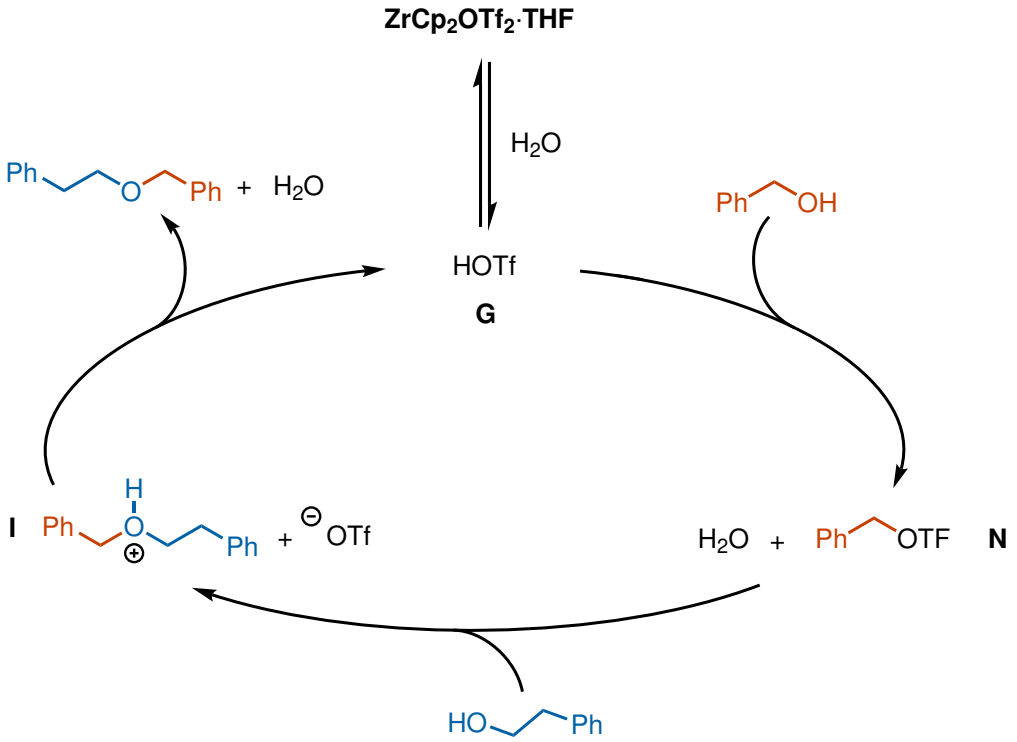

Figure 26: Proposed catalytic cycle in which $ZrCp_2OTf_2 \cdot THF$ acts as a precatalyst, releasing HOTf, which can then react with the alcohol to form a triflate intermediate. This intermediate sets the stage for a subsequent attack by a second alcohol.

The proposed mechanism would commence with the hydrolysis of $ZrCp_2OTf_2 \cdot THF$, yielding HOTF. Subsequently, BnOTf is formed, which can be trapped by PhEtOH. The subsequent regeneration of HOTF and the release of ether would close the catalytic cycle.
The energy profile for the reaction is shown in Figure 27. The formation of BnOTf was found to be in an energetically favorable range ($\Delta G^{\ddagger}$(**G**$_{\textbf{no-water}}$→**N**) = 29.9 kcal/mol). Moreover, the subsequent attack of either BnOH ($\Delta G^{\ddagger}$(**N**→**I**$_{\textbf{BnOH}}$) = 29.1 kcal/mol) or PhEtOH ($\Delta G^{\ddagger}$(**N**→**I**$_{\textbf{PhEtOH}}$) = 29.4 kcal/mol) falls within the same energetic range. Additionally, the formation of PhEtOTf was studied more closely, showing that it is energetically less favorable compared to the formation of BnOTf($\Delta G^{\ddagger}$(**O**→**P**) = 33.4 kcal/mol). The following substitution of OTf with BnOH or PhEtOH resulted in a energetic barrier of $\Delta G^{\ddagger}$(**P**→**R**$_{\textbf{PhEtOH}}$) = 33.8 kcal/mol for the attack of PhEtOH and $\Delta G^{\ddagger}$(**P**→**R**$_{\textbf{BnOH}}$) = 34.2kcal/mol for BnOH.

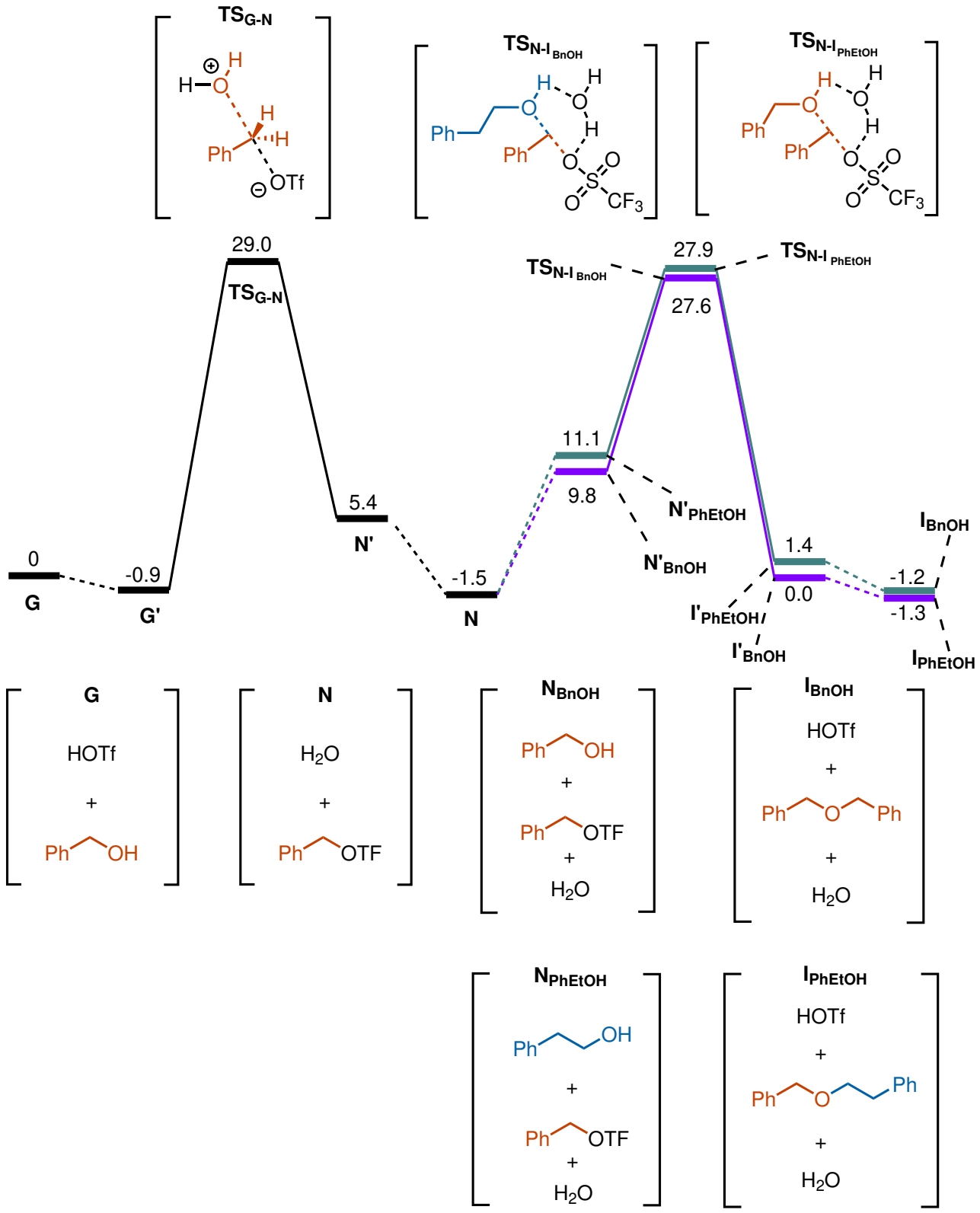

Figure 27: Energy profile (relative Gibbs free energies ($\Delta G_{373\,K,\,toluene}$ [kcal/mol]) for the formation of BnOTf followed by the nucleophilic attack of BnOH (purple)or PhEtOH (green). Reactant and product complexes are labeled with an apostrophe. The sum of the reactant energies is taken as a reference (0.0 kcal/mol). Level of theory: DLPNO-CCSD(T)-CPCM(toluene)/def2-TZVP//ωB97XD-CPCM(toluene)/def2-SVP.

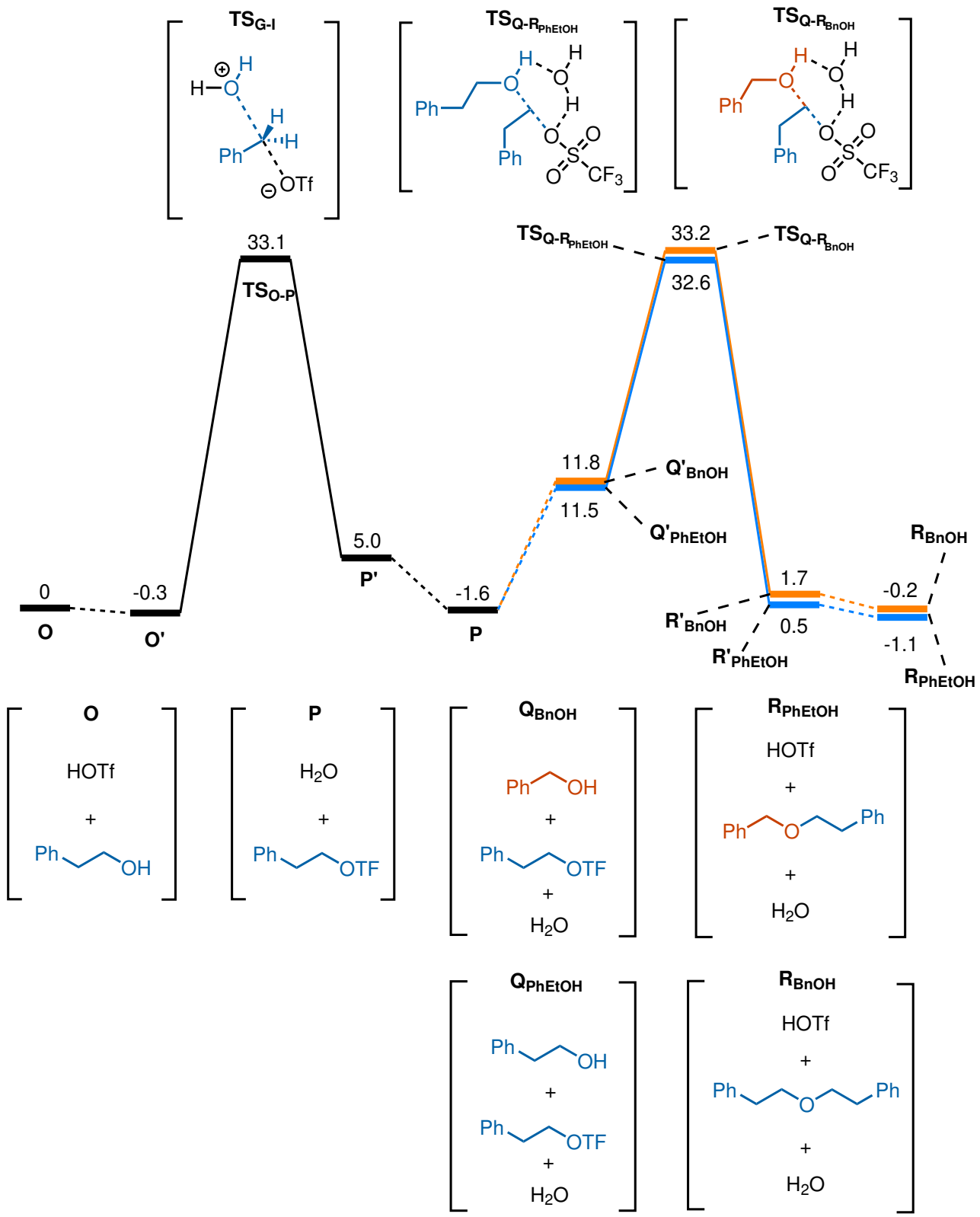

Figure 28: Energy profile (relative Gibbs free energies ($\Delta G_{373\,K,\,toluene}$ [kcal/mol]) for the formation of PhEtOTf followed by the nucleophilic attack of BnOH (orange) or PhEtOH (blue).Reactant and product complexes are labeled with an apostrophe. The sum of the reactant energies is taken as a reference (0.0 kcal/mol). Level of theory: DLPNO-CCSD(T)-CPCM(toluene)/def2-TZVP//ωB97XD-CPCM(toluene)/def2-SVP.

8 Conclusion

An *in silico* investigation was carried out to examine the zirconocene catalyst $ZrCp_2OTf_2 \cdot THF$ and its possible involvement in direct alcohol substitution, resulting in an etherification reaction. To ensure an accurate description of the catalytic system, a benchmark study was performed to determine a reliable theoretical model. Furthermore, prior to any mechanistic studies, several zirconocene complexes were compared to identify the catalytically important species. The investigation revealed that the exchange of triflate ligands is an unfavorable process. Additionally, NBO charges analysis did not indicate any significant activation of BnOH or PhEtOH after their coordination to the complex. Based on these results, different mechanistic pathways have been considered:

1. A thorough examination of an S_N2-like reaction, involving the coordination of an alcohol to the complex followed by an attack by a second alcohol, was carried out. However, this mechanistic pathway was found to be energetically unfavourable. Moreover, the addition of water to facilitate proton transfer not only failed to lower the reaction barrier but also had the opposite effect.

2. Additionally, the investigation delved into the C-O bond cleavage of BnOH coordinated to a zirconocene triflate. However, it was determined that the formation of a carbocation in this context had an even higher energy barrier than the previously studied nucleophilic substitution-like reaction. Furthermore, the formation of a BnOTf species following the mentioned C-O bond cleavage was found to be energetically unfavourable as well.

3. An alternative approach with the hydrolysis of $ZrCp_2OTf_2 \cdot THF$ leading to the release of HOTf, which could act as the actual catalyst, was also studied. It was indeed found that HOTf can catalyze the reaction by protonating the alcohol, thereby activating it for the subsequent nucleophilic attack by a second alcohol. Furthermore, it was demonstrated that an OTf anion is also capable of performing this nucleophilic substitution reaction. The subsequently formed triflate can also be attacked by a second alcohol in a feasible range to produce the ether as a product. For all reactions, it was shown that BnOH is preferred to act as the electrophile, and PhEtOH as the nucleophile.

Considering all these results, this theoretical investigation suggests that $ZrCp_2OTf_2 \cdot THF$ functions as a precatalyst which is able to release HOTf, which in turn can catalyze the reaction as a Brønsted acid. However, a comprehensive understanding of the complete mechanism requires a detailed examination of the precise pathway leading to HOTf in the composition reaction. Furthermore, there is a need for experimental evidence supporting the formation of HOTf.

References

[1] Marian C. Bryan, Peter J. Dunn, David Entwistle, Fabrice Gallou, Stefan G. Koenig, John D. Hayler, Matthew R. Hickey, Shaun Hughes, Michael E. Kopach, Gerard Moine, Paul Richardson, Frank Roschangar, Alan Steven, and Franz J. Weiberth. Key green chemistry research areas from a pharmaceutical manufacturers' perspective revisited. *Green Chem.*, 20:5082–5103, 2018.

[2] Robert W. Dugger, John A. Ragan, and David H. Brown Ripin. Survey of gmp bulk reactions run in a research facility between 1985 and 2002. *Organic Process Research & Development*, 9(3):253–258, 2005.

[3] Benjamin G. Reed-Berendt, Daniel E. Latham, Mubarak B. Dambatta, and Louis C. Morrill. Borrowing hydrogen for organic synthesis. *ACS Central Science*, 7(4):570–585, 2021. PMID: 34056087.

[4] Qin Yang, Qingfu Wang, and Zhengkun Yu. Substitution of alcohols by n-nucleophiles via transition metal-catalyzed dehydrogenation. *Chem. Soc. Rev.*, 44:2305–2329, 2015.

[5] Fei Huang, Zhuqing Liu, and Zhengkun Yu. C-alkylation of ketones and related compounds by alcohols: Transition-metal-catalyzed dehydrogenation. *Angewandte Chemie International Edition*, 55(3):862–875, 2016.

[6] Kumar Rakesh and Erik Van der Eycken. Recent approaches for c–c bond formation via direct dehydrative coupling strategies. *Chem. Soc. Rev.*, 42:1121–1146, 2013.

[7] Enrico Emer, Riccardo Sinisi, Montse Guiteras Capdevila, Diego Petruzziello, Francesco De Vincentiis, and Pier Giorgio Cozzi. Direct nucleophilic sn1-type reactions of alcohols. *European Journal of Organic Chemistry*, 2011(4):647–666, 2011.

[8] Marco Bandini and Michele Tragni. pi-activated alcohols: an emerging class of alkylating agents for catalytic friedel–crafts reactions. *Org. Biomol. Chem.*, 7:1501–1507, 2009.

[9] Cristiana Margarita and Davide Di Francesco. Catalytic dehydrative transformations mediated by moisture-tolerant zirconocene triflate. *Synlett*, 2023.

[10] Cristiana Margarita, Piret Villo, Hernando Tuñon, Oscar Dalla-Santa, David Camaj, Robin Carlsson, Malin Lill, Anja Ramström, and Helena Lundberg. Zirconium-catalysed direct substitution of alcohols: enhancing the selectivity by kinetic analysis. *Catal. Sci. Technol.*, 11:7420–7430, 2021.

[11] Cristiana Margarita, Davide Di Francesco, Hernando Tuñon, Ivan Kumaniaev, Carlos Jansson Rada, and Helena Lundberg. Mild and selective etherification of wheat straw lignin and lignin model alcohols by moisture-tolerant zirconium catalysis. *Green Chem.*, 25:2401–2408, 2023.

[12] Douglas R. Hartree. The wave mechanics of an atom with a non-coulomb central field. part ii. some results and discussion. *Mathematical Proceedings of the Cambridge Philosophical Society*, 24(1):111–132, 1928.

[13] Frank Jensen. *Introduction to computational chemistry*. John wiley & sons, 2017.

[14] Christian Møller and Milton S. Plesset. Note on an approximation treatment for many-electron systems. *Phys. Rev.*, 46:618–622, Oct 1934.

[15] Christopher J. Cramer. *Essentials of computational chemistry: theories and models*. John Wiley & Sons, 2013.

[16] Jeremy Harvey. *Computational chemistry*. Oxford University Press, 2018.

[17] Yang Guo, Christoph Riplinger, Ute Becker, Dimitrios G. Liakos, Yury Minenkov, Luigi Cavallo, and Frank Neese. Communication: An improved linear scaling perturbative triples correction for the domain based local pair-natural orbital based singles and doubles coupled cluster method [DLPNO-CCSD(T)]. *The Journal of Chemical Physics*, 148(1):011101, 01 2018.

[18] P. Hohenberg and W. Kohn. Inhomogeneous electron gas. *Phys. Rev.*, 136:B864–B871, Nov 1964.

[19] Axel D. Becke. A new mixing of Hartree–Fock and local density-functional theories. *The Journal of Chemical Physics*, 98(2):1372–1377, 01 1993.

[20] Riffat Parveen, Thomas R. Cundari, Jarod M. Younker, and George Rodriguez. Computational assessment of counterion effect of borate anions on ethylene polymerization by zirconocene and hafnocene catalysts. *Organometallics*, 39(11):2068–2079, 2020.

[21] Stefan Grimme. Semiempirical gga-type density functional constructed with a long-range dispersion correction. *Journal of Computational Chemistry*, 27(15):1787–1799, 2006.

[22] Stefan Grimme, Stephan Ehrlich, and Lars Goerigk. Effect of the damping function in dispersion corrected density functional theory. *Journal of Computational Chemistry*, 32(7):1456–1465, 2011.

[23] Axel D. Becke. Density-functional thermochemistry. V. Systematic optimization of exchange-correlation functionals. *The Journal of Chemical Physics*, 107(20):8554–8560, 11 1997.

[24] Stefan Grimme, Andreas Hansen, Jan Gerit Brandenburg, and Christoph Bannwarth. Dispersion-corrected mean-field electronic structure methods. *Chemical Reviews*, 116(9):5105–5154, 2016. PMID: 27077966.

[25] Stefan Grimme. Density functional theory with london dispersion corrections. *WIREs Computational Molecular Science*, 1(2):211–228, 2011.

[26] Aleksandr V. Marenich, Christopher J. Cramer, and Donald G. Truhlar. Universal solvation model based on solute electron density and on a continuum model of the solvent defined by the bulk dielectric constant and atomic surface tensions. *The Journal of Physical Chemistry B*, 113(18):6378–6396, 2009. PMID: 19366259.

[27] Maurizio Cossi, Nadia Rega, Giovanni Scalmani, and Vincenzo Barone. Energies, structures, and electronic properties of molecules in solution with the c-pcm solvation model. *Journal of Computational Chemistry*, 24(6):669–681, 2003.

[28] Vincenzo Barone and Maurizio Cossi. Quantum calculation of molecular energies and energy gradients in solution by a conductor solvent model. *The Journal of Physical Chemistry A*, 102(11):1995–2001, 1998.

[29] Markus Bursch, Jan-Michael Mewes, Andreas Hansen, and Stefan Grimme. Best-practice dft protocols for basic molecular computational chemistry**. *Angewandte Chemie International Edition*, 61(42):e202205735, 2022.

[30] Sebastian Spicher and Stefan Grimme. Robust atomistic modeling of materials, organometallic, and biochemical systems. *Angewandte Chemie International Edition*, 59(36):15665–15673, 2020.

[31] Vincenzo Barone and Maurizio Cossi. Quantum calculation of molecular energies and energy gradients in solution by a conductor solvent model. *The Journal of Physical Chemistry A*, 102(11):1995–2001, 1998.

[32] Frank Neese. The orca program system. *WIREs Computational Molecular Science*, 2(1):73–78, 2012.

[33] Jeng-Da Chai and Martin Head-Gordon. Long-range corrected hybrid density functionals with damped atom–atom dispersion corrections. *Phys. Chem. Chem. Phys.*, 10:6615–6620, 2008.

[34] Jeng-Da Chai and Martin Head-Gordon. Systematic optimization of long-range corrected hybrid density functionals. *The Journal of Chemical Physics*, 128(8):084106, 02 2008.

[35] John P. Perdew, Kieron Burke, and Matthias Ernzerhof. Generalized gradient approximation made simple. *Phys. Rev. Lett.*, 77:3865–3868, Oct 1996.

[36] John P. Perdew, Kieron Burke, and Matthias Ernzerhof. Reply: Generalized gradient approximation made simple. *Phys. Rev. Lett.*, 80:891–891, Jan 1998.

[37] Carlo Adamo and Vincenzo Barone. Toward reliable density functional methods without adjustable parameters: The PBE0 model. *The Journal of Chemical Physics*, 110(13):6158–6170, 04 1999.

[38] Chengteh Lee, Weitao Yang, and Robert G. Parr. Development of the colle-salvetti correlation-energy formula into a functional of the electron density. *Phys. Rev. B*, 37:785–789, Jan 1988.

[39] Florian Weigend and Reinhart Ahlrichs. Balanced basis sets of split valence, triple zeta valence and quadruple zeta valence quality for h to rn: Design and assessment of accuracy. *Phys. Chem. Chem. Phys.*, 7:3297–3305, 2005.

[40] Dmitrij Rappoport and Filipp Furche. Property-optimized Gaussian basis sets for molecular response calculations. *The Journal of Chemical Physics*, 133(13):134105, 10 2010.

[41] Philipp Pracht, Fabian Bohle, and Stefan Grimme. Automated exploration of the low-energy chemical space with fast quantum chemical methods. *Phys. Chem. Chem. Phys.*, 22:7169–7192, 2020.

[42] Stefan Grimme. Exploration of chemical compound, conformer, and reaction space with meta-dynamics simulations based on tight-binding quantum chemical calculations. *Journal of Chemical Theory and Computation*, 15(5):2847–2862, 2019. PMID: 30943025.

[43] Stefan Grimme. Supramolecular binding thermodynamics by dispersion-corrected density functional theory. *Chemistry – A European Journal*, 18(32):9955–9964, 2012.

[44] Yi-Pei Li, Joseph Gomes, Shaama Mallikarjun Sharada, Alexis T. Bell, and Martin Head-Gordon. Improved force-field parameters for qm/mm simulations of the energies of adsorption for molecules in zeolites and a free rotor correction to the rigid rotor harmonic oscillator model for adsorption enthalpies. *The Journal of Physical Chemistry C*, 119(4):1840–1850, 2015.

[45] Guilian Luchini, Robert Paton, Juanvi Alegre-Requena, Jaime Rodríguez-Guerra, Eric Berquist, JingTao Chen, IFunes, Julia Velmiskina, froessler, Heather Mayes, Shree Sowndarya Santhanalakkshmi Vejaykummar, and sibo. patonlab/goodvibes: Bug fixes & updated references. *GitHub*, August 2022.

[46] James P. Foster and Frank Weinhold. Natural hybrid orbitals. *Journal of the American Chemical Society*, 102(24):7211–7218, 1980.

[47] Alan E. Reed, Larry A. Curtiss, and Frank Weinhold. Intermolecular interactions from a natural bond orbital, donor-acceptor viewpoint. *Chemical Reviews*, 88(6):899–926, 1988.

[48] Thibaut Courant, Marine Gavel, Romain M. Q. Renard, Vincent Gandon, Antoine Y. P. Joosten, and Thomas Lecourt. Zirconium-catalyzed hydroalumination of co bonds: Site-selective de-o-acetylation of peracetylated compounds and mechanistic insights. *The Journal of Organic Chemistry*, 86(14):9280–9288, 2021. PMID: 34125557.

[49] Steven M. Maley, Graham R. Lief, Richard M. Buck, Orson L. Sydora, Qing Yang, Steven M. Bischof, and Daniel H. Ess. Density functional theory and ccsd(t) evaluation of ionization potentials, redox potentials, and bond energies related to zirconocene polymerization catalysts. *Journal of Computational Chemistry*, 44(4):506–515, 2023.

[50] Jan Gerit Brandenburg, Georg Bender, Jinjun Ren, Andreas Hansen, Stefan Grimme, Hellmut Eckert, Constantin G. Daniliuc, Gerald Kehr, and Gerhard Erker. Crystal packing induced carbon–carbon double–triple bond isomerization in a zirconocene complex. *Organometallics*, 33(19):5358–5364, 2014.

[51] Sankaranarayanapillai Shylesh, Lance A. Bettinson, Ahmed Aljahri, Martin Head-Gordon, and Alexis T. Bell. Experimental and computational studies of carbon–carbon bond formation via ketonization and aldol condensation over site-isolated zirconium catalysts. *ACS Catalysis*, 10(8):4566–4579, 2020.

[52] Yuelong Tian, Weigang Zhang, Min Ge, Shouquan Yu, Xiaoxu Lv, and Tingting Zhang. Polymerization of methylsilylenes into polymethylsilanes or polycarbosilanes after dechlorination of dichloromethylsilanes? *RSC Adv.*, 6:21048–21055, 2016.

[53] Joyce Y. Corey, Xiao-Hong. Zhu, Lee Brammer, and Nigam P. Rath. Zirconocene Dichloride. *Acta Crystallographica Section C*, 51(4):565–567, Apr 1995.

[54] Ulf Thewalt and Wiltraud Lasser. Fünffach koordinierte zirkonium(iv)-komplexe mit der (eta -c5h5)2zriv-baueinheit. die struktur von (eta -c5h5)2zr(cf3so3)2(thf) / five coordinate zirconium(iv) complexes with the (eta-c5h5)2zriv unit. the structure of (eta-c5h5)2zr(cf3so3)2(thf). *Zeitschrift für Naturforschung B*, 38(11):1501–1505, 1983.

[55] Alireza Abbasi, Patric Lindqvist-Reis, Lars Eriksson, Dick Sandström, Sven Lidin, Ingmar Persson, and Magnus Sandström. Highly hydrated cations: Deficiency, mobility, and coordination of water in crystalline nonahydrated scandium(iii), yttrium(iii), and lanthanoid(iii) trifluoromethanesulfonates. *Chemistry – A European Journal*, 11(14):4065–4077, 2005.

[56] Pierre-Adrien Payard, Qingyi Gu, Wenping Guo, Qianran Wang, Matthieu Corbet, Carine Michel, Philippe Sautet, Laurence Grimaud, Raphael Wischert, and Marc Pera-Titus. Direct amination of alcohols catalyzed by aluminum triflate: An experimental and computational study. *Chemistry – A European Journal*, 24(53):14146–14153, 2018.

[57] Masahiro Noji, Tomoko Ohno, Koji Fuji, Noriko Futaba, Hiroyuki Tajima, and Keitaro Ishii. Secondary benzylation using benzyl alcohols catalyzed by lanthanoid, scandium, and hafnium triflate. *The Journal of Organic Chemistry*, 68(24):9340–9347, 2003. PMID: 14629155.

[58] Enrico Emer, Riccardo Sinisi, Montse Guiteras Capdevila, Diego Petruzziello, Francesco De Vincentiis, and Pier Giorgio Cozzi. Direct nucleophilic sn1-type reactions of alcohols. *European Journal of Organic Chemistry*, 2011(4):647–666, 2011.

[59] Ivan Šolić, Pattarakiat Seankongsuk, Joanna Kejun Loh, Tirayut Vilaivan, and Roderick W. Bates. Scandium as a pre-catalyst for the deoxygenative allylation of benzylic alcohols. *Org. Biomol. Chem.*, 16:119–123, 2018.

9 Appendices

Table 3: Absolute difference of experimentally measured and theoretically calculated Zr-Cl, Zr-Cp, Zr-OTf, and Zr-THF bond lengths with different levels of theory.

Level of Theory	Zr-Cl	Zr-Cp	Zr-OTf	Zr-THF
PBE0-D3/def2-SVP	0.009	0.007	0.037	0.029
PBE0-D3/def2-SVPD	0.001	0.002	0.013	0.017
PBE0-D3/def2-TZVP	0.009	0.01	0.013	0.021
B3LYP-D3/def2-SVP	0.002	0.039	0.033	0.026
B3LYP-D3/def2-SVPD	0.018	0.034	0.005	0.011
B3LYP-D3/def2-TZVP	0.007	0.045	0.004	0.019
ωB97XD/def2-SVP	0.006	0.011	0.022	0.030
ωB97XD/def2-SVPD	0.022	0.008	0.005	0.019
ωB97XD/def2-TZVP	0.007	0.014	0.005	0.023

Table 4: Absolute difference of experimentally measured and theoretically calculated Cl-Zr-Cl, Cp-Zr-Cp, and fTO-Zr-OTf bond angles with different levels of theory.

Level of Theory	Cl-Zr-Cl	Cp-Zr-Cp	fTO-Zr-OTf
PBE0-D3/def2-SVP	1.4	0.2	4.8
PBE0-D3/def2-SVPD	1.4	0.3	5.4
PBE0-D3/def2-TZVP	1.2	0.3	5.3
B3LYP-D3/def2-SVP	1.1	0.3	5.5
B3LYP-D3/def2-SVPD	1.1	0.4	6.2
B3LYP-D3/def2-TZVP	1.0	0.4	6.0
ωB97XD/def2-SVP	1.0	0.4	4.6
ωB97XD/def2-SVPD	1.2	0.7	5.0
ωB97XD/def2-TZVP	0.6	0.8	4.8

Level of Theory	Zr-Cl	Zr-Cp	Zr-OTf	Zr-THF
ωB97XD-SMD/def2-SVP	0.006	0.011	0.022	0.003
ωB97XD-CPCM/def2-SVP	0.002	0.008	0.023	0.031

Table 5: Absolute difference of experimentally measured and theoretically calculated Zr-Cl, Zr-Cp, Zr-OTf, and Zr-THF bond lengths with different solvation models.

Level of Theory	Cl-Zr-Cl	Cp-Zr-Cp	fTO-Zr-OTf
ωB97-SMD/def2-SVP	4.6	0.4	1.0
ωB97XD-CPCM/def2-SVP	4.4	0.36	0.7

Table 6: Absolute difference of experimentally measured and theoretically calculated Cl-Zr-Cl, Cp-Zr-Cp, and fTO-Zr-OTf bond angles with different solvation models.